





REVIEW

Open Access



# Heterogeneous rheology of Japan subduction zone revealed by postseismic deformation of the 2011 Tohoku-oki earthquake

Sambuddha Dhar<sup>1\*</sup> , Jun Muto<sup>1</sup> , Yusaku Ohta<sup>2,3</sup>  and Takeshi Iinuma<sup>4</sup> 

## Abstract

The 2011 Tohoku-oki earthquake produced the most well-recorded postseismic deformation of any megathrust earthquake in the world. Over the last decade, researchers have used a dense and widespread geodetic network of more than 1300 Global Navigation Satellite System (GNSS) stations inland, as well as the about 50 stations on the seafloor, to investigate the various deformation sources responsible for the observed crustal deformation. One of the contributing mechanisms to this crustal deformation is the stress relaxation of the viscoelastic mantle beneath the Japanese arc. As evident in experimental rock physics and geophysical observations, ambient mantle conditions and related rheology are expected to be heterogeneous in space. However, the contribution of such rheological heterogeneities to the postseismic deformation is still poorly understood. Here, we piece together several rheological heterogeneities inferred from the decade-long postseismic deformation of the 2011 Tohoku-oki earthquake. We reviewed more than twenty postseismic models to understand how viscoelastic earth can influence the postseismic surface deformation observed after the Tohoku-oki earthquake. Besides, we employed several synthetic models to tease out the contribution of individual rheological heterogeneities such as depth-dependent rheology of mantle wedge, oceanic asthenosphere, and low-viscosity zone beneath the volcanic front. We demonstrate that the vertical postseismic observation is the key to unravel rheological complexity beneath northeastern Japan. The broader vertical deformation pattern reveals the major viscosity contrast between backarc and forearc, and small-scale subsidence detects the presence of low-viscosity bodies related to arc magmatism. In short, this review paper provides a vista of three-dimensional heterogeneous rheology of viscoelastic earth. These rheological heterogeneities may play a crucial role in bridging the gap between our understanding of different phase of subduction zone earthquake cycle.

**Keywords** Postseismic deformation, GNSS observations, Viscoelastic relaxation, Afterslip, Nonlinear rheology, Earthquake deformation cycle, Rheological heterogeneity

\*Correspondence:

Sambuddha Dhar  
sambuddha.dhar.p8@dc.tohoku.ac.jp

<sup>1</sup> Department of Earth Science, Tohoku University, 6-3 Aoba, Aoba-Ku, Aramaki, Sendai, Japan

<sup>2</sup> Research Center for Prediction of Earthquakes and Volcanic Eruptions, Graduate School of Science, Tohoku University, 6-6 Aza-Aoba, Aoba-Ku, Aramaki, Sendai 980-8578, Japan

<sup>3</sup> Division for the Establishment of Frontier Sciences of Organization for Advanced Studies, Tohoku University, 2-1-1 Katahira, Aoba-Ku, Sendai, Japan

<sup>4</sup> Japan Agency for Marine-Earth Science and Technology, 3173-25 Showa-Machi, Kanazawa-Ku, Yokohama, Japan

## 1 Introduction

Since the Mw 9 Tohoku-oki earthquake hit northeastern (NE) Japan on March 11, 2011, dense and widespread geodetic network terrestrial Global Navigation Satellite System (GNSS) and seafloor GNSS-Acoustic ranging combination technique (GNSS-A) stations have captured postseismic crustal deformation at unprecedented high resolution in time and space (Ozawa et al. 2012; Watanabe et al. 2014, 2021; Sun et al. 2014; Tomita et al. 2017; Yokota et al. 2018; Honsho et al. 2019). From 1994 to the present, a nationwide GNSS network has provided a

continuous record of interseismic, coseismic, and post-seismic deformation of the 2011 Tohoku-oki earthquake (e.g., Kato et al. 1998; Sagiya et al. 2000; Nishimura et al. 2004; Ozawa et al. 2012; Nishimura 2014; Sagiya and Meneses-Gutierrez 2022). In addition, another local GNSS network has been monitoring crustal deformation at high resolution around the Tohoku district. Together, these inland networks reveal crucial information on postseismic deformation following the 2011 Tohoku-oki earthquake (Muto et al. 2016, 2019; Dhar et al. 2022), as well as the 2008 Iwate-Nairiku earthquake (Ohta et al. 2008; Iinuma et al. 2009; Ohzono et al. 2012). Moreover, the remarkable near-field observations made immediately after the earthquake by seafloor geodesy installed above the main rupture area provide a unique opportunity to shed light on the viscoelastic process (Sato et al. 2011; Kido et al. 2011; Sun et al. 2014; Watanabe et al. 2014; Iinuma et al. 2016), which has not been available for other megathrust earthquakes in subduction zones such as Chile, Sumatra, and Cascadia.

During the megathrust rupture, significant coseismic stress is imparted on the plate boundary fault and surrounding crust and mantle. The weaker part of the lower crust-upper mantle initiates a viscoelastic flow to relax the perturbed stress (i.e., viscoelastic relaxation, hereafter VR) and a continuous aseismic slip (i.e., afterslip, hereafter AS) is triggered on the megathrust interface. VR is perceived to be a long-term deformation on a decadal to centennial scale (Nur and Mavko 1974), such as postglacial rebound (James et al. 2000) or long-term postseismic deformation (e.g., 1964 Alaska earthquake, Suito and Freymueller 2009). However, after the 2004 Sumatra earthquake, several studies have inferred the necessity of VR to explain postseismic deformation immediately after the mainshock (e.g., Pollitz et al. 2006; Han et al. 2008; Hoechner et al. 2011). AS is perceived to cause the short-term postseismic deformation near the rupture zone (e.g., Marone et al. 1991; Wennerberg and Sharp 1997; Heki et al. 1997; Hsu et al. 2006; Pritchard and Simons 2006). Since the seafloor geodesy provided unambiguous evidence for the domination of transient viscoelastic flow immediately after the 2011 Tohoku-oki earthquake (Sun et al. 2014; Watanabe et al. 2014), recent postseismic models of the earthquake have combined VR and AS to explain the postseismic deformation (Diao et al. 2014; Shirzaei et al. 2014; Sun et al. 2014; Yamagiwa et al. 2015; Sun and Wang 2015; Hu et al. 2016; Freed et al. 2017; Suito 2017; Wang et al. 2018; Agata et al. 2019; Muto et al. 2016, 2019; Fukuda and Johnson 2021; Dhar et al. 2022).

The rheological properties of viscoelastic earth have also been conceptualized through the laboratory experiments on rocks (Karato and Jung 2003; Hirth and

Kohlstedt 2003; Bürgmann and Dresen 2008; Muto 2011). Freed and Bürgmann (2004) pioneered the inference of the nonlinear rheological properties of the Mojave Desert mantle from the postseismic observations of the 1992 Landers and 1999 Hector Mine earthquakes in southern California. Since then, the application of laboratory-derived constitutive properties of rocks to various postseismic observations has provided a unique opportunity to illuminate heterogeneous lithosphere–asthenosphere rheology originating from the spatial variation of the ambient deformation conditions, such as temperature, water content, and grain size (Freed et al. 2006, 2010, 2012; Masuti et al. 2016; Tang et al. 2019, 2020).

Since the deployment of a dense nationwide seismic network around 2000 (Okada et al. 2004; Obara et al. 2005), detailed seismic structures in the Japan subduction zone have been investigated. These observations as well as other geophysical observations such as magnetotelluric (Ogawa et al. 2014) and geothermal gradients (Tanaka et al. 2004; Matsumoto et al. 2022), have provided information on the structures and ambient conditions of the island arc mantle wedge and subducting Pacific plate overlying oceanic mantle in NE Japan. Such information on the subduction zone can be used to infer the rheological heterogeneity of NE Japan based on the postseismic deformation of the 2011 Tohoku-oki earthquake (e.g., Muto et al. 2013). Hence, we piece together the rheological heterogeneities inferred by postseismic models developed over the last decade (Fig. 1). We reviewed the role of these rheological heterogeneities in the postseismic crustal deformation shortly after the megathrust earthquake. We also qualitatively evaluated the geodetically inferred rheology from the perspective of experimental rock physics and various geophysical observations around NE Japan. Here, Sects. 2 and 3 summarize 10 years of GNSS observations after the 2011 Tohoku-oki earthquake and the constitutive properties of rock reported by laboratory experiments, respectively. In Sect. 4, we introduce several synthetic models (including the weaker part of the mantle wedge and oceanic mantle) to investigate how heterogeneous rheology controls the pattern of postseismic surface deformation. Our study primarily focuses on numerical modeling using power-law rheology which can explain postseismic deformation from the perspective of rock mechanics. Section 5 presents a detailed analysis of the rheological heterogeneities inferred by several postseismic models developed over the past decade.

## 2 Decade-long geodetic constraints

### 2.1 Geodetic dataset

Here, we reviewed geodetic observations around NE Japan over the past decade. The locations of inland and seafloor GNSS stations around NE Japan are summarized

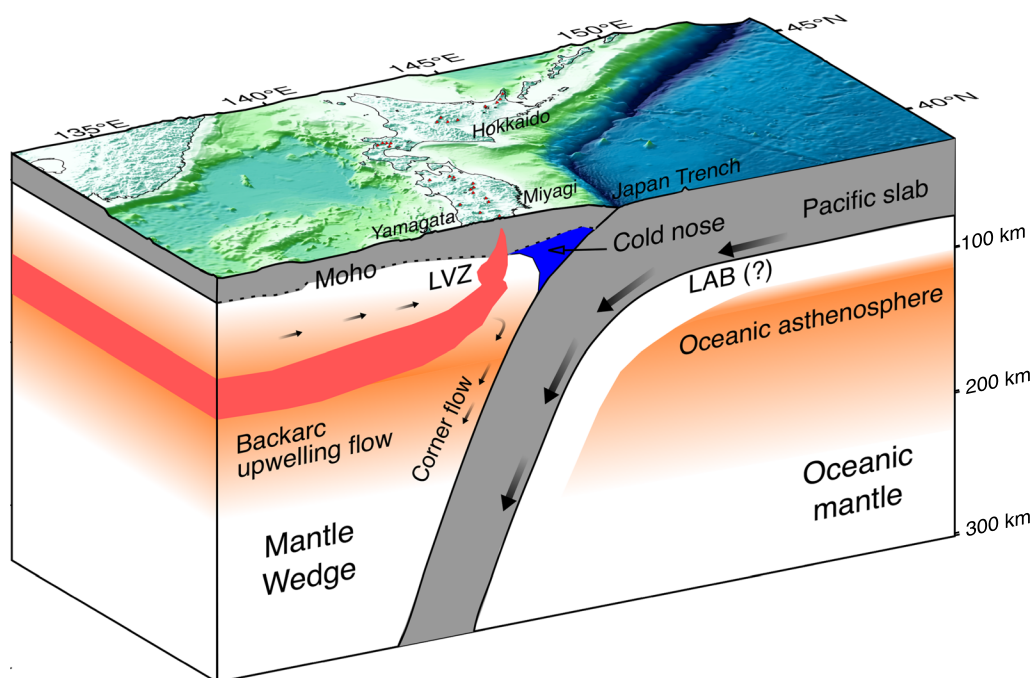


**Fig. 1** Schematic diagram for heterogeneous rheology of NE Japan revealed by decade-long geodetic observation after the 2011 Tohoku-oki earthquake. The shape of upper surface of Pacific plate is adopted from Nakajima and Hasegawa (2006) and Nakajima et al. (2009). Qualitative colormap of viscosity marked blue for high viscosity and red for low viscosity. See main text for further details

in Fig. 2a. In Japanese archipelagoes, crustal deformation has been monitored by the GNSS Earth Observation Network System (GEONET), a dense and widespread network of ~1300 permanent GNSS stations maintained by the Geospatial Information Authority of Japan since 1994 (e.g., Sagiya et al. 2000). In addition, a network of ~64 GNSS stations operated by Tohoku University has been recording the crustal deformation in Iwate, Miyagi, Yamagata, Fukushima, and Niigata prefectures (Ohta et al. 2008; Ohzono et al. 2012; Muto et al. 2016, 2019; Dhar et al. 2022). Compared to an average site spacing of 20–25 km for GEONET, Tohoku University's network has an average site spacing of ~10 km, providing a much denser geodetic network (hereafter, THK site).

Since 2000, the Japan Coast Guard (JCG) has been conducting GNSS-A seafloor geodetic observations at five stations installed on the landward slope of the Japan Trench (Fig. 2a and Additional file 1: Fig. S1). Currently, the JCG can provide observations for each site three times a year with precision in centimeters (Ishikawa et al. 2020). Four of these JCG sites are located directly above the main rupture area of the 2011 Tohoku-oki earthquake leading to crucial observations of the postseismic deformations during the 10 years following the earthquake (Sato et al. 2011; Watanabe et al. 2014, 2021). In addition, the Tohoku University's research group also conducted several campaign GNSS-A observations (from

September 2012 to September 2016) at 20 sites (hereafter, TU GNSS-A sites; Fig. 2a and Additional file 1: Fig. S1) installed near the Japan Trench (Kido et al. 2015; Tomita et al. 2015, 2017; Honsho et al. 2019). Following the earthquake, the vertical deformation near the JCG site above the main rupture area was captured by seven ocean bottom pressure (OBP) gauges, which were also operated by Tohoku University, as reported by Iinuma et al. (2016).

## 2.2 GNSS observations

Figure 2b–d shows the average displacement rates of the onshore and offshore NE Japan during 2011–2014, 2014–2017, and 2017–2020. As expected from any megathrust earthquake (Pollitz et al. 2008; Panet et al. 2010; Wang et al. 2012), the terrestrial observations displayed a wholesale trenchward movement in approximately the same direction as the coseismic displacements (Ozawa et al. 2011, 2012). The rapid trenchward motion is observed in the early years (Fig. 2b) but decrease substantially in the later period (Fig. 2c, d). After 2014, the trenchward motion in the Kanto region and the southern part of Fukushima prefecture significantly decreases (westward motion in Fig. 2c) and displays a landward movement in the observations from 2017 to 2020 (Fig. 2d). The landward motion may be influenced by continuing strong northwest motion of fully coupled

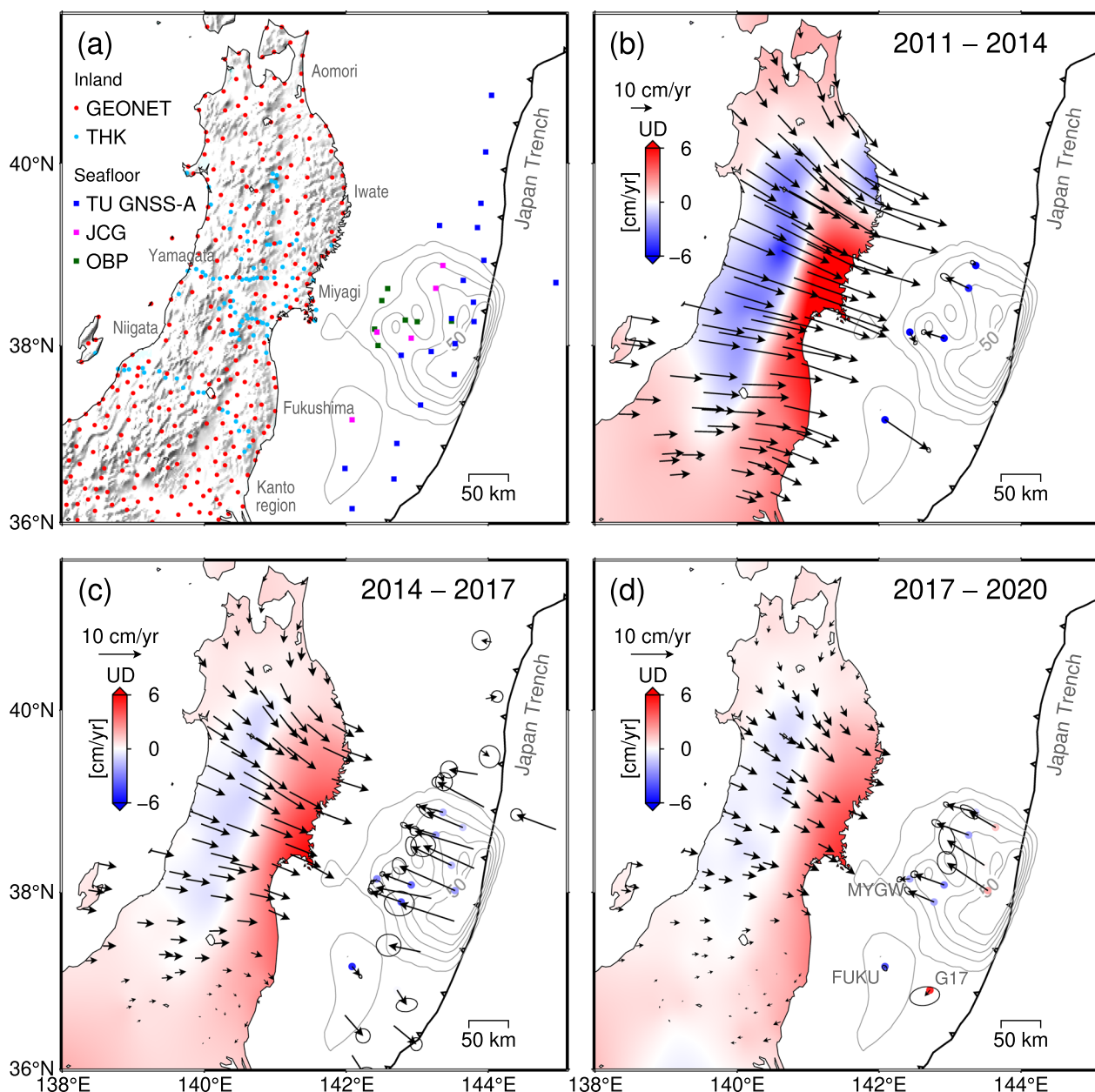


**Fig. 2** Decade-long geodetic observations after the 2011 Tohoku-oki earthquake around NE Japan. **a** The location of onshore and offshore geodetic stations. **b** Displacement rate during April 2011–April 2014, **c** April 2014–April 2017, and **d** April 2017–April 2020. Note that only high-quality data of 110 GEONET stations is plotted and horizontal motion during 2011–2014 is scale down to one half in **(b)**. The displacement rate at JCG and TU GNSS-A sites is opted from Honsho et al. (2019) and Watanabe et al. (2021). The displacements of inland GNSS stations are referenced to Fukue station (ID: 950,462; 128.843°E, 32.669°N)

Philippines Sea slab (Suito 2018); however, further analysis is required to understand it clearly. As per the observations from 2017 onward, the eastern part of Aomori prefecture also displays a southwest motion. Although the westward motion can be influenced by interseismic plate coupling at Aomori-oki, our understanding of such plate coupling is still limited.

A few seafloor JCG sites (MYGI, KAMS, KAMN) and an OBP site (GJT3) show landward motion (Sun et al. 2014; Watanabe et al. 2014; see Additional file 1: Fig. S1a for site names of seafloor observations) shortly after the mainshock. These landward displacements provide unique evidence that VR dominates short-term postseismic deformation (e.g., Sun et al. 2014; Sun and

Wang 2015). Notably, the MYGW station redirected its motion toward land in ~2017 onward (Watanabe et al. 2021). Before ~2014, the motion of KAMN was significantly slower than that of its neighboring stations (KAMS and MYGI); however, after ~2014, the movement of KAMN became consistent with them. The JCG site FUKU and a few TU sites (G17, G18, G19, and G20) along Fukushima-oki exhibited a rapid seaward motion during 2011–2017 (Tomita et al. 2017; Honsho et al. 2019; Watanabe et al. 2021).

The postseismic vertical deformation shows pronounced subsidence at the volcanic front to backarc and rapid uplift along the Pacific coast in the central Tohoku district (~100-km wavelength). In addition, the THK network provided a high-resolution dataset that displays local-scale subsidence around the volcanic region, which is stronger than the background subsidence (Muto et al. 2016). Several models have explained this deformation pattern by incorporating rheological heterogeneities such as the cold nose in the forearc and low-viscosity zone (LVZ) at the volcanic front (discussed in detail later). This heterogeneity of the mantle wedge was inferred only by the models that employed both horizontal and vertical geodetic constraints (Hu et al. 2014; Muto et al. 2016, 2019; Luo and Wang 2021; Dhar et al. 2022). Most postseismic studies have concluded that the vertical deformation pattern is sensitive to the complex rheological structure beneath NE Japan (Hu et al. 2014, 2016; Freed et al. 2017; Suito 2017; Muto et al. 2016, 2019; Fukuda and Johnson 2021; Luo and Wang 2021). By using both horizontal and vertical displacements, several studies have inferred heterogeneous rheology models such as depth-dependent rheology, LVZs at the volcanic front to the backarc, or cold nose in the forearc mantle wedge (Freed et al. 2017; Suito 2017; Muto et al. 2016, 2019; Luo and Wang 2021; Dhar et al. 2022).

### 3 Laboratory-derived constitutive laws of rocks

Laboratory experiments on rocks representing the lower crust and upper mantle suggest viscoelastic behavior in response to applied stress. When a constant stress is instantaneously applied under a pressure and temperature equivalent to depth, a rock displays an initial elastic response followed by a rapid strain-rate change (transient deformation) with a subsequent constant strain rate (steady state) deformation. Figure 3a shows a schematic diagram of rock deformations inferred from laboratory experiments. In the steady state, a viscoelastic material under the most plausible experimental conditions shows a power-law dependence of stress on strain rate (e.g., Goetze and Evans 1979; Kirby 1983; Shimamoto 1993; Kohlstedt et al. 1995; Bürgmann and Dresen 2008; Karato 2008). The steady-state flow law incorporates thermally activated deformation processes in the following form (Kirby and Kronenberg 1987; Carter and Tsenn 1987; Karato and Jung 2003; Hirth and Kohlstedt 2003; Bürgmann and Dresen 2008; Muto 2011):

$$\dot{\epsilon} = A(C_{OH})^r d^{-m} \sigma^n \exp\left(-\frac{Q + p\Omega}{RT}\right), \quad (1)$$

where  $\dot{\epsilon}$  is the strain rate,  $A$  is the pre-exponential factor,  $Q$  is the activation energy,  $\Omega$  is the activation volume,  $n$  is the power-law exponent,  $p$  is the pressure,  $T$  is the absolute temperature,  $R$  is the gas constant,  $d$  is the grain size,  $m$  is the grain-size exponent,  $C_{OH}$  is the water content,  $r$  is the water-content exponent, and  $\sigma$  is the differential stress. The stress exponent  $n$  depends on the microscopic deformation mechanisms (Hirth and Kohlstedt 2003; Bürgmann and Dresen 2008) that govern the plastic flow of rocks. If the flow is accommodated by dislocation creep,  $n$  tends to be between 2 and 4, whereas  $n$  is 1 for diffusion creep. Laboratory experiments suggest that dislocation creep predominantly governs the mantle flow under relatively high-stress conditions. The prevalence of

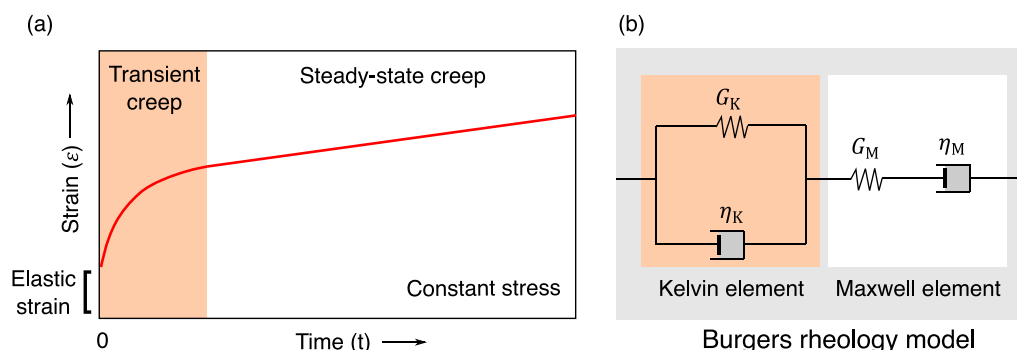


**Fig. 3** Schematic diagrams of the transient deformation of rocks under constant stress. **a** The time-dependent strain of mantle rock under constant stress. **b** Spring–dashpot representation of biviscous (Burgers) rheology.  $G_K$  and  $G_M$  denote shear modulus of the Kelvin element and the Maxwell element, respectively.  $\eta_K$  and  $\eta_M$  represent viscosity of the Kelvin element and the Maxwell element, respectively

dislocation creep in upper mantle can be substantiated by observations of seismic anisotropy owing to the preferred orientation of olivine minerals (Silver et al. 1999). Under a low-stress regime, diffusion creep dominates the mantle flow.

From Eq. (1), effective viscosity ( $\eta^{eff} = \sigma/2\dot{\epsilon}$ ) can be expressed as follows:

$$\eta^{eff} = \frac{1}{2}A^{-1}(C_{OH})^{-r}d^m\sigma^{1-n}\exp\left(\frac{Q+p\Omega}{RT}\right) \quad (2)$$

With a power-law rheology of  $n=2-4$ , the effective viscosity depends on the magnitude of the stress given by a background stress (or pre-stress) and coseismic stress change. Therefore, coseismic stress changes significantly decrease the viscosity. For example, shortly after a megathrust rupture, the effective viscosity in the surrounding lower crust/upper mantle is temporarily reduced under high stress caused by coseismic events, leading to a rapid postseismic strain rate of deformation (i.e., transient creep). Over time, stress is dissipated owing to the continuous viscous flow (stress relaxation), restoring the pre-earthquake effective viscosity under steady-state stress (background stress or pre-stress). For Newtonian rheology with  $n=1$ , the effective viscosity is independent of stress.

Experiments on olivine (single crystal or aggregates) also indicate the reduction in viscosity by several orders of magnitude (compared to steady state) at the onset of transient creep (Post 1977; Smith and Carpenter 1987; Chopra 1997; Hanson and Spetzler 1994; Hansen et al. 2021). This rapid change of viscosity is due to the initial strain increments which may result from microstructural evolution such as changes in distribution and arrangement of dislocations (Durham et al. 1977; Hanson and Spetzler 1994). The transient creep may attribute to the increase in dislocation density (e.g., Durham et al. 1977) until it becomes constant under the applied stress. At constant dislocation densities, the dislocation structure may require additional strain to overcome the threshold strength and evolve again (strain hardening). The transient creep of olivine has been explained by several micro-mechanical processes, including intergranular mechanism (Ashby and Duval 1985; Karato 1998, 2021; Masuti et al. 2019) and elastic resistance to dislocation movement (Hansen et al. 2019).

The transient deformation of natural rock can be understood as the acceleration of the strain rate in the early phase of rock deformation (Fig. 3a). Burgers rheology model (a spring–dashpot system) is a widely used phenomenological representation of transient and steady-state deformation (Carter and Kirby 1978; Smith and Carpenter 1987; Chopra 1997; Karato 2008; Masuti and Barbot 2021). Burgers model consists of two

elements: Kelvin and Maxwell elements, which represent the transient and steady-state deformations, respectively (Fig. 3b). Kelvin element includes a spring and dashpot connected in parallel, whereas Maxwell element comprises a spring and a dashpot joined in series. The strain rate in the spring of Maxwell element, dashpot of Maxwell element, and dashpot of Kelvin element indicates the initial elastic response, steady-state viscous flow, and rapid transient viscous flow, respectively. As transient and steady-state deformations occur simultaneously, the strain due to the transient and steady-state deformations is connected in series. For Burgers rheology, the strain rate ( $\dot{\epsilon}$ ) as a function of time ( $t$ ) can be expressed as follows (Karato 2008, 2021; Freed et al. 2012):

$$\dot{\epsilon} = \dot{\epsilon}_0 + (\dot{\epsilon}_{ST} - \dot{\epsilon}_0)\left[1 - e^{-\frac{t}{\tau}}\right], \quad (3)$$

where  $\tau$  is the transient relaxation time,  $\dot{\epsilon}_0$  is the initial strain rate,  $\dot{\epsilon}_{ST}$  is the steady-state strain rate. The above equation can be rewritten as follows:

$$\dot{\epsilon} = \dot{\epsilon}_{ST}\left[1 - e^{-\frac{t}{\tau}} + \beta e^{-\frac{t}{\tau}}\right], \quad (4)$$

where  $\beta(= \dot{\epsilon}_0/\dot{\epsilon}_{ST})$  indicates the ratio of the steady-state viscosity to transient viscosity and can be used to control the transient deformation. Notably, the transient relaxation time can be directly related to the transient viscosity (transient viscosity = transient relaxation time  $\times$  shear modulus), regardless of linear or nonlinear rheology. Alternatively, several studies (Qiu et al. 2018; Tang et al. 2019; Weiss et al. 2019; Agata et al. 2019; Muto et al. 2019; Dhar et al. 2022) have adopted the strain rate as a function of the evolving stress (time-independent form), which can be expressed as follows:

$$\dot{\epsilon} = \frac{\sigma^n}{\eta_M} + \frac{(\sigma - 2G_K\epsilon_K)^n}{\eta_K}, \quad (5)$$

where  $\sigma$  represents the differential stress at each time step including the pre-stress and coseismic stress change,  $\eta_M$  represents the steady-state viscosity (i.e., Maxwell viscosity),  $\eta_K$  is the transient viscosity (i.e., Kelvin viscosity),  $n$  is the stress exponent,  $G_K$  is the strain hardening coefficient, and  $\epsilon_K$  is the cumulative transient strain due to strain hardening. The physical significance of parameter  $G_K$  is poorly understood from an experimental perspective (Masuti et al. 2016, 2019; Masuti and Barbot 2021).

Although the transient viscosity of mantle rock has not been experimentally studied in detail, the ratio of steady state to transient viscosity is usually considered constant. Experiments on olivine suggest a value of 2–10 (Carter and Ave'Lllemant 1970; Post 1977; Mackwell et al. 1985; Chopra 1997). Using transient rheology, the values of the ratio inferred from previous postseismic models were

4–10 (1999 M7.6 Izmit earthquake; Hearn et al. 2009), 29 (1999 Hector Mine; Pollitz 2003), 10 (1999 Hector Mine; Freed et al. 2010), 1.5–6 (1999 Hector Mine; Freed et al. 2012), 29 (2002 M7.9 Denali earthquake; Pollitz 2005), 20 (2004 Sumatra earthquake; Pollitz et al. 2006, 2008), 10–100 (series of Sumatran earthquakes; Qiu et al. 2018), and 10 (1999 Chi-Chi earthquake; Tang et al. 2019). The adaptation of its value also varies widely for postseismic models developed after the 2011 Tohoku-oki earthquake. Several postseismic models have inferred the values of 1 (Agata et al. 2019), 6 (Muto et al. 2016), 10 (Hu et al. 2016; Muto et al. 2019; Dhar et al. 2022), and 25 (Fukuda and Johnson 2021).

The postseismic GNSS time series of large earthquakes including the 2011 Tohoku-oki earthquake displays biphasic surface deformation including rapid transient deformation, followed by steady-state deformation. This biphasic deformation is well explained by biviscous Burgers rheology (e.g., Pollitz 2003) as well as power-law rheology (e.g., Freed and Bürgmann 2004). Several studies have also combined transient creep and power-law flow to explain the postseismic geodetic observations of the 1999 Hector Mine earthquake (Freed et al. 2010, 2012) or 2004 Sumatra earthquake (Masuti et al. 2016) and 2011 Tohoku-oki earthquake (Agata et al. 2019; Muto et al. 2019; Dhar et al. 2022). Morikami and Mitsui (2020) utilized high-rate GNSS observations (horizontal directions) following the 2011 Tohoku-oki earthquake and inferred that ground displacement rate follows an Omori-like power-law decay (non-Maxwellian deformation) immediately after the earthquake. Compared with the decaying trend of aftershock occurrence ( $p$ -value  $\sim 1$ ), a slower decay of horizontal ground motion with a  $p$ -value of  $\sim 0.69$  indicates biviscous Burgers rheology or power-law rheology rather than Maxwell rheology (Ingleby and Wright 2017).

## 4 Controls of heterogeneous rheology on postseismic deformation

### 4.1 Base postseismic models

In this study, we constructed a simple two-dimensional (2-D) rheological model to test the effect of various rheological structures near the main rupture area of the 2011 Tohoku-oki earthquake. Similar approaches have been used in several previous studies (Sun and Wang 2015; Yabe et al. 2015; Muto et al. 2016; Luo and Wang 2022). Sun and Wang (2015) revealed that postseismic horizontal motion is sensitive to the contribution of both the mantle wedge and the oceanic asthenosphere. Conversely, similar models by Luo and Wang (2022) demonstrate that the mantle wedge and oceanic mantle independently cause the vertical motion above the forearc and trench areas, respectively. Using a 2-D

rheology model, we investigated the controls of heterogeneous rheology such as depth-dependent viscosity, LVZ, and oceanic asthenosphere, on postseismic deformation across NE Japan. First, we built a base viscoelastic model (Fig. 4a) composed of a mantle wedge and oceanic mantle with uniform viscosities and an elastic cold nose (similar to Sun et al. 2014; Luo and Wang 2021; Fukuda and Johnson 2021). The thicknesses of the continental crust and Pacific slab are 30 km and 50 km, respectively. We adopted the Maxwell viscosities of the oceanic mantle of  $1.1 \times 10^{20}$  Pa·s and mantle wedge of  $5.6 \times 10^{18}$  Pa·s from Fukuda and Johnson (2021). The ratio between Maxwell and Kelvin viscosities is 25 (Fukuda and Johnson 2021). The model framework (Fig. 4a) and coseismic slip distribution (Additional file 1: Fig. S1b) were used the same as those used by Dhar et al. (2022) and Inuma et al. (2012), respectively. The postseismic deformation was simulated using the integral methods with in-plane strain conditions (Lambert and Barbot 2016; Barbot et al. 2017; Barbot 2018; Muto et al. 2019; Dhar et al. 2022). As our base model considers neither interseismic plate coupling nor AS displacements, we calculated 3 years of postseismic surface deformation using only VR. Consistent with the most previous postseismic model (listed in Table 1), our base viscoelastic model produces an opposing trenchward and landward motion above land and near-trench areas, respectively (Fig. 4a). The displacement field of the viscoelastic mantle over the 3 years of postseismic deformation is illustrated by flow vectors (arrows in Fig. 4a). The mantle-flow vectors show two opposing flow patterns due to the asymmetric nature of the coseismic deformation (Sun and Wang 2015). The base viscoelastic model with linear Burgers rheology (blue line in Fig. 4a) produces a weak sub-arc uplift, strong coastal uplift, and near-trench uplift, similar to the results of several previous linear models (Luo and Wang 2021, 2022; Fukuda and Johnson 2021). The details of model structures are summarized in Additional file 1: Table S1. Notably, the presence of a cold nose causes a significant reduction in horizontal motion and substantial uplift above the coastal areas, as reported by Luo and Wang (2021).

Changing the linear rheology to power-law one not only suppresses the horizontal motion but also adds subsidence at the volcanic front and more uplift in coastal areas (hereafter, base model displacement, black line in Fig. 4a). The mantle flow in power-law rheology exhibits a similar pattern to that in linear rheology but with less magnitude, except for the part of the mantle close to the coseismic rupture zone (Fig. 4a). Compared to the linear model, the lower magnitude of postseismic displacements in the power-law model are likely due to the localization of viscous deformation closer to the coseismic rupture zone where the viscosity is significantly reduced by the

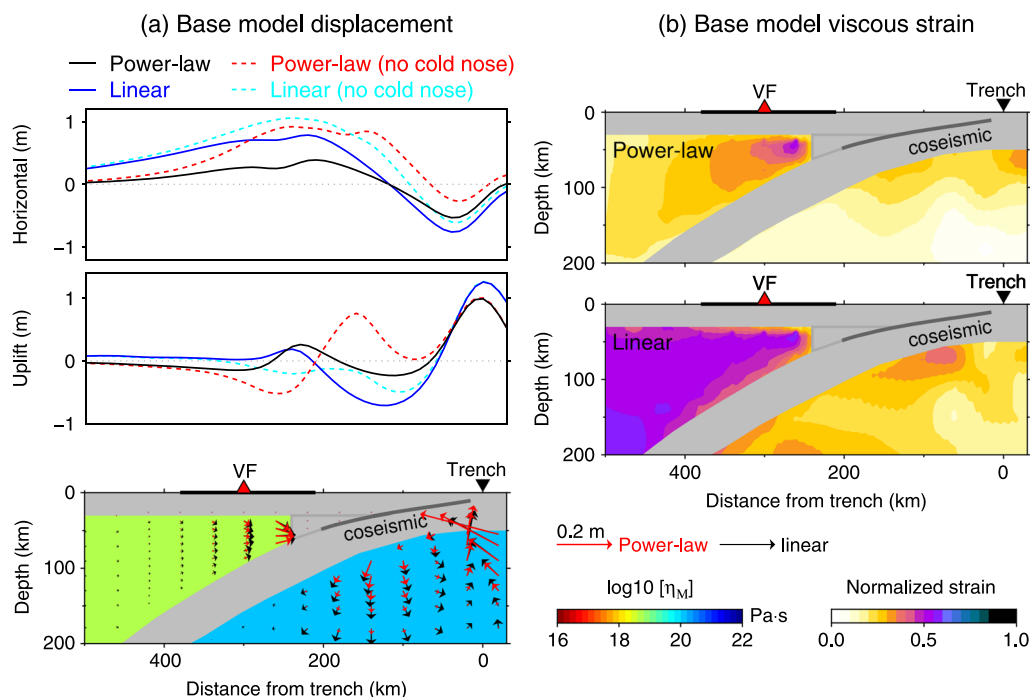


**Fig. 4** The effect of base viscoelastic model on the 3-year postseismic deformation. **a** The surface displacement by base viscoelastic models with linear and power-law rheology. The surface displacements by base model without cold nose are illustrated by dotted lines. The 2-D viscosity profile depict the basic viscoelastic model with uniform viscosities for upper mantle and oceanic mantles. The flow vectors for power-law and linear model are also illustrated. **b** The viscous strains calculated over 3 years of postseismic deformation in the power-law and linear base models. The strain distribution is normalized by coseismic strain perturbation (normalized strain = total strain / coseismic strain change). Viscous strain is defined as the second invariant of the deviatoric strain tensor

coseismic stress change (see viscous strain distributions in Fig. 4b). In particular, the effective viscosities (steady-state and transient deformation) of the mantle close to the coseismic rupture zone are reduced by one to two orders of magnitude immediately after the earthquake (Fig. 5). However, they gradually increase over time as stress relaxation progresses. Figure 5a–f illustrates the evolution of effective viscosities for the power-law base model. The details on the calculation of effective viscosities are provided in Additional file 1: Text S1.

#### 4.2 Depth-dependent viscosity model

Experimental rock physics has suggested viscosity stratification in the lithosphere–asthenosphere due to the temperature and pressure dependences of rocks (i.e., depth-dependent rheology) (Turcotte and Schubert 1982; Hirth and Kohlstedt 2003; Riva and Govers 2009). Equation 2 shows that the viscosity decreases as the temperature increases, whereas the viscosity increases as the pressure increases (for a constant value of other rheological parameters). The rapid increase in temperature across the lithosphere as a thermal boundary layer causes a sharp drop in viscosity. Beneath the lithosphere, although the temperature rises along an adiabat, the viscosity

increases with depth by the pressure dependence via activation volume (Eq. 2). The steady-state viscosity profile indicates that the region of minimum viscosity at a depth of ~100–150 km may be associated with the asthenosphere.

To investigate the effect of depth-dependent rheology, we built a one-dimensional temperature- and pressure-dependent viscosity profile using the flow law of olivine (Karato and Jung 2003; see also Additional file 1). The thermal structure is calculated using a half-space cooling model (Turcotte and Schubert 1982; see also Dhar et al. 2022). In the model with the depth-dependent viscosity profile in the mantle wedge (Fig. 6), changes are noticeable in the magnitude, but not in the pattern of horizontal motion compared to the power-law base model. Although horizontal motion is sensitive to both rheology of mantle wedge and oceanic mantle, the mantle wedge rheology largely affects the inland vertical motion (Luo and Wang 2022). The depth-dependent viscosity structure produces additional uplift above the coastal area. We evaluated the surface displacements for five depth-dependent viscosity models with different activation volumes and water contents (Fig. 6; see also Additional file 1: Table S2). The values of activation volume and



**Table 1** Summary of postseismic models of the M9 2011 Tohoku-oki earthquake

Reference	Rheology model	Geodetic constraint	Mantle wedge viscosity [Pa-s] [+ Cold nose (CN)]	Upper crust/ Pacific slab [km/km]	Oceanic mantle viscosity [Pa-s]	Oceanic asthenosphere [Pa-s] [+ LAB]
Imakiire and Koarai (2012)	E	Horizontal 0–4 month	NA NA	NA	NA	NA
Ozawa et al. (2012)	E	Horizontal 0–9 month	NA NA	NA	NA	NA
Perfettini and Avouac (2014)	E	Horizontal 0–9 month	NA NA	NA	NA	NA
Silverii et al. (2014)	E	Horizontal 0–4 month	NA NA	NA	NA	NA
Diao et al. (2014)	LM	Horizontal 0–18 month	Layered earth $2 \times 10^{19}$ ( $\eta_M$ ) [+ No CN]	50/No	Layered earth $1 \times 10^{20}$ ( $\eta_M$ )	Layered earth $2 \times 10^{19}$ ( $\eta_M$ ) [+ No LAB]
Yamagiwa et al. (2015)	LM	Horizontal & vertical 0.6–18 month 0.6–9.6 month 1.6–9.6 month	Layered earth $9 \times 10^{18}$ ( $\eta_M$ ) [+ No CN]	50/No	Layered earth $1 \times 10^{20}$ ( $\eta_M$ )	Layered earth $9 \times 10^{18}$ ( $\eta_M$ ) [+ No LAB]
Freed et al. (2017)	LM	Horizontal & vertical 0–36 month	Heterogeneous* $10^{18} - 10^{19}$ ( $\eta_M$ ) [+ Viscous CN]	30/60	$\sim 3 \times 10^{19}$ ( $\eta_M$ )	$\sim 9 \times 10^{18}$ ( $\eta_M$ ) [+ LAB $\sim 3 \times 10^{18}$ ( $\eta_M$ )]
Suito (2017)	LM	Horizontal & vertical 0–60 month	Heterogeneous* $\sim 2 \times 10^{18}$ ( $\eta_M$ ) [+ Viscous CN]	30/80	$1 \times 10^{19}$ ( $\eta_M$ )	$1 \times 10^{19}$ ( $\eta_M$ ) [+ LAB $\sim 1 \times 10^{18}$ ( $\eta_M$ )]
Muto et al. (2016)	LB	Horizontal & vertical 0–9 month	Heterogeneous* $\sim 10^{18}$ ( $\eta_M$ ) [+ Viscous CN]	20/60	Heterogeneous* $\sim 10^{19}$ ( $\eta_M$ )	Heterogeneous* $\sim 10^{19}$ ( $\eta_M$ ) [+ LAB $\sim 5 \times 10^{18}$ ( $\eta_M$ )]
Sun et al. (2014)	LB	Horizontal 0–12 month	$1.8 \times 10^{18}$ ( $\eta_M$ ) $2.5 \times 10^{17}$ ( $\eta_K$ ) [+ Elastic CN]	25/25	$1 \times 10^{20}$ ( $\eta_M$ ) $2 \times 10^{18}$ ( $\eta_K$ )	$1 \times 10^{20}$ ( $\eta_M$ ) $2 \times 10^{18}$ ( $\eta_K$ ) [+ LAB $2.5 \times 10^{17}$ ( $\eta_{M,K}$ )]
Shirzaei et al. (2014)	LB	Horizontal 0–15 month	$1 \times 10^{19}$ ( $\eta_M$ ) $1 \times 10^{18}$ ( $\eta_K$ ) [+ No CN]	50/50	$1 \times 10^{20}$ ( $\eta_M$ ) $1 \times 10^{19}$ ( $\eta_K$ )	$1 \times 10^{20}$ ( $\eta_M$ ) $1 \times 10^{19}$ ( $\eta_K$ ) [+ No LAB]
Sun and Wang (2015)	LB	Horizontal 0–36 month	$1.8 \times 10^{18}$ ( $\eta_M$ ) $2.5 \times 10^{17}$ ( $\eta_K$ ) [+ Elastic CN]	25/45	$1 \times 10^{20}$ ( $\eta_M$ ) $2 \times 10^{18}$ ( $\eta_K$ )	$1 \times 10^{20}$ ( $\eta_M$ ) $2 \times 10^{18}$ ( $\eta_K$ ) [+ LAB $2.5 \times 10^{17}$ ( $\eta_{M,K}$ )]
Iinuma et al. (2016)	LB	Horizontal & vertical 0–9 month	$1.8 \times 10^{18}$ ( $\eta_M$ ) $2.5 \times 10^{17}$ ( $\eta_K$ ) [+ Elastic CN]	25/45	$1 \times 10^{20}$ ( $\eta_M$ ) $2 \times 10^{18}$ ( $\eta_K$ )	$1 \times 10^{20}$ ( $\eta_M$ ) $2 \times 10^{18}$ ( $\eta_K$ ) [+ LAB $2.5 \times 10^{17}$ ( $\eta_{M,K}$ )]
Hu et al. (2014)	LB	Horizontal & vertical 0–12 month	$1 \times 10^{19}$ ( $\eta_M$ ) $1 \times 10^{18}$ ( $\eta_K$ ) [+ No CN]	40/80	$1 \times 10^{20}$ ( $\eta_M$ ) $1 \times 10^{19}$ ( $\eta_K$ )	$1 \times 10^{20}$ ( $\eta_M$ ) $1 \times 10^{19}$ ( $\eta_K$ ) [+ No LAB]
Hu et al. (2016)	LB	Horizontal & vertical 0–24 month	$3 \times 10^{19}$ ( $\eta_M$ ) $3 \times 10^{18}$ ( $\eta_K$ ) [+ Elastic CN]	40/80	$5 \times 10^{19}$ ( $\eta_M$ ) $5 \times 10^{18}$ ( $\eta_K$ )	$\sim 10^{18}$ ( $\eta_M$ ) $\sim 10^{17}$ ( $\eta_K$ ) [+ No LAB]
Wang et al. (2018)	LB	Horizontal & vertical 0–60 month	$1.8 \times 10^{18}$ ( $\eta_M$ ) $2.5 \times 10^{17}$ ( $\eta_K$ ) [+ Elastic CN]	25/45	$1 \times 10^{20}$ ( $\eta_M$ ) $2 \times 10^{18}$ ( $\eta_K$ )	$1 \times 10^{20}$ ( $\eta_M$ ) $2 \times 10^{18}$ ( $\eta_K$ ) [+ LAB $2.5 \times 10^{17}$ ( $\eta_{M,K}$ )]
Fukuda and Johnson (2021)	LB	Horizontal & vertical 0–84 month	$5.6 \times 10^{18}$ ( $\eta_M$ ) $2.2 \times 10^{17}$ ( $\eta_K$ ) [+ Elastic CN]	30/50	$\sim 1.2 \times 10^{20}$ ( $\eta_M$ ) $\sim 4.5 \times 10^{18}$ ( $\eta_K$ )	$\sim 1.2 \times 10^{20}$ ( $\eta_M$ ) $\sim 4.5 \times 10^{18}$ ( $\eta_K$ ) [+ No LAB]
Luo and Wang (2021, 2022)	LB	Horizontal & vertical 0–60 month	$4.5 \times 10^{18}$ ( $\eta_M$ ) $1 \times 10^{18}$ ( $\eta_K$ ) [+ Elastic CN]	30/45	$5 \times 10^{19}$ ( $\eta_M$ ) $5 \times 10^{18}$ ( $\eta_K$ )	$5 \times 10^{19}$ ( $\eta_M$ ) $5 \times 10^{18}$ ( $\eta_K$ ) [+ No LAB]
Agata et al. (2019)	NLB	Horizontal 0–33 month	Heterogeneous* $\sim 10^{19}$ ( $\eta_M$ ) $\sim 10^{19}$ ( $\eta_K$ ) [+ Elastic CN]	40/100 (?)	Heterogeneous* $\sim 10^{19}$ ( $\eta_M$ ) $\sim 10^{19}$ ( $\eta_K$ )	$\sim 10^{19}$ ( $\eta_M$ ) $\sim 10^{19}$ ( $\eta_K$ ) [+ No LAB]

**Table 1** (continued)

Reference	Rheology model	Geodetic constraint	Mantle wedge viscosity [Pa·s] [+ Cold nose (CN)]	Upper crust/Pacific slab [km /km]	Oceanic mantle viscosity [Pa·s]	Oceanic asthenosphere [Pa·s] [+ LAB]
Muto et al. (2019)	NLB	Horizontal & vertical 0–63 month	Heterogeneous* $10^{16} - 10^{20}$ ( $\eta_M$ ) $10^{15} - 10^{19}$ ( $\eta_K$ ) [+ Viscous CN]	20/60	Heterogeneous $10^{16} - 10^{20}$ ( $\eta_M$ ) $10^{15} - 10^{19}$ ( $\eta_K$ )	$\sim 1 \times 10^{18}$ ( $\eta_M$ ) $\sim 1 \times 10^{16}$ ( $\eta_K$ ) [+ No LAB]
Dhar et al. (2022)	NLB	Horizontal & vertical 0–63 month	Heterogeneous* $10^{17} - 10^{20}$ ( $\eta_M$ ) $10^{16} - 10^{19}$ ( $\eta_K$ ) [+ Viscous CN]	20/60	Heterogeneous* $10^{17} - 10^{20}$ ( $\eta_M$ ) $10^{16} - 10^{19}$ ( $\eta_K$ )	$\sim 1 \times 10^{20}$ ( $\eta_M$ ) $\sim 1 \times 10^{19}$ ( $\eta_K$ ) [+ No LAB]

E Elastic, LM linear Maxwell, LB linear Burgers, NLB nonlinear Burgers, LAB lithosphere–asthenosphere boundary

\*For heterogeneous model, average viscosities are displayed

water content are carefully chosen so that the minimum Maxwell viscosities reach the value of either  $5.6 \times 10^{16}$ ,  $5.6 \times 10^{17}$ , or  $5.6 \times 10^{18}$  Pa·s. Figure 6a compares the sur-

of the weak layer (at  $\sim 50$ – $100$  km depth; Fig. 6a–b) in the depth-dependent viscosity model (see Additional file 1: Fig. S2), which significantly changes the surface displace-

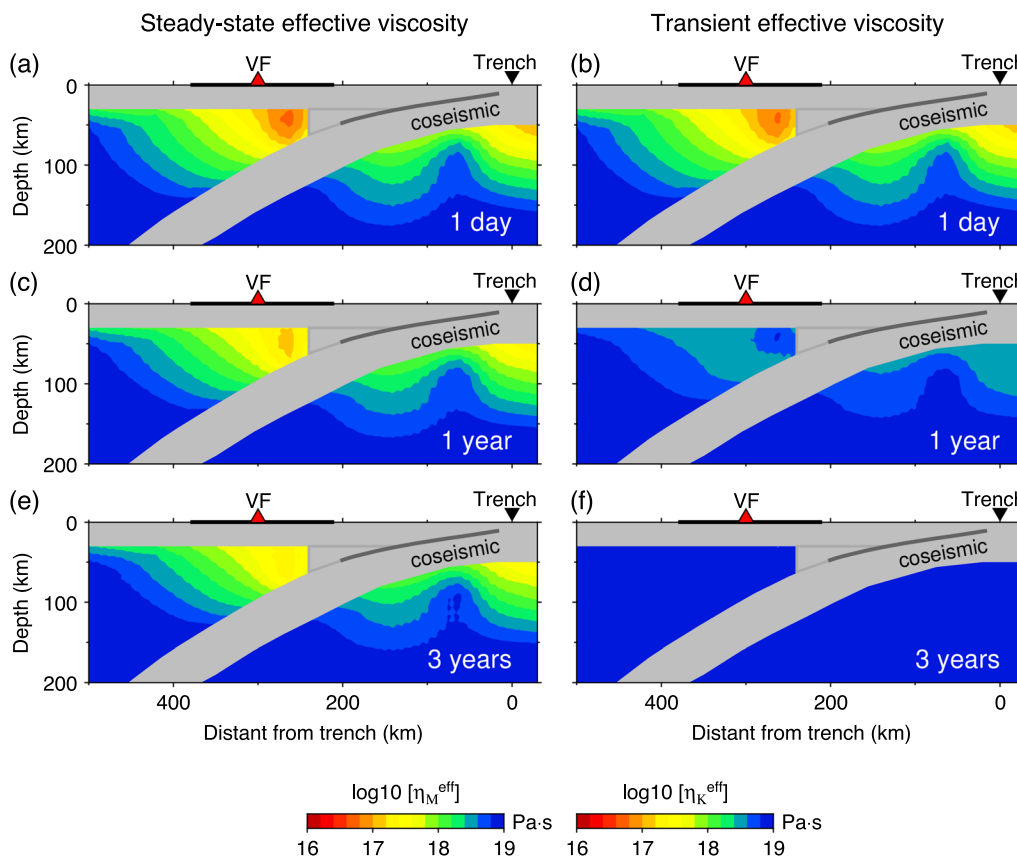


**Fig. 5** The postseismic evolution of effective viscosity in the power-law base model. The effective viscosities of steady-state (Maxwell element; left panel) and transient (Kelvin element; right panel) deformation are shown for **a–b** 1 day, **c–d** 1 year, **e–f** 3 years after the earthquake

face displacements by the models where the activation volume is different, but the water content is fixed. The change in the activation volume (with a fixed water content) affects both the width and the minimum viscosity

ment pattern. Similarly, Fig. 6b illustrates the surface displacements by the models with various water contents under fixed activation volume. The change in water content (with a fixed activation volume) affects the viscosity

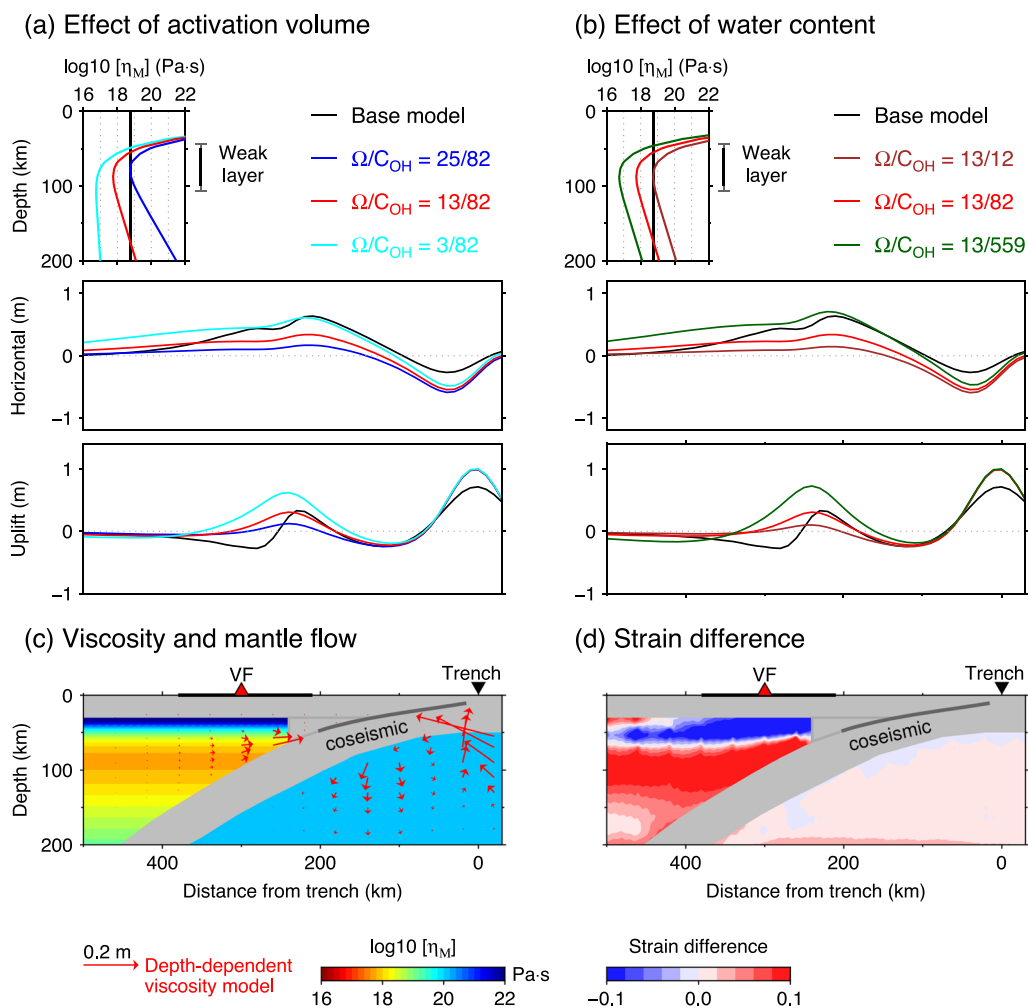


**Fig. 6** The effect of depth-dependent viscosity on the 3-year postseismic deformation. **a** The surface displacement in mantle wedge where activation volume  $\Omega$  vary 25, 13, and 3  $\text{cm}^3/\text{mol}$  with a fixed water content  $C_{\text{OH}}$  of  $\sim 82$  ppm H/Si. The corresponding 1-D viscosity profiles are shown in top panel. **b** The surface displacement by the model where  $C_{\text{OH}}$  vary as  $\sim 12, \sim 82$ , and  $\sim 559$  ppm H/Si with fixed  $\Omega$  of  $\sim 13$   $\text{cm}^3/\text{mol}$ . The corresponding 1-D viscosity profiles are displayed in top panel. See model details in Additional file 1: Table S2. **c** The trench-normal profile shows the viscosity distribution and mantle flow pattern for the model with  $\Omega = \sim 13$   $\text{cm}^3/\text{mol}$  and  $C_{\text{OH}} = 82$  ppm H/Si are shown. **d** The distribution of strain difference corresponds to the model shown in (c). Strain difference = strain in the depth-dependent model – strain in the base model. All viscous strain (second invariant of the deviatoric strain tensor) is normalized by the coseismic strain

substantially but not the width of the weak layer. Either through changing activation volume or water content, the rheology that employs the same minimum viscosity results in a similar surface deformation pattern. This indicates that the surface deformation pattern is sensitive to the viscosity of weakest layer in depth-dependent models. The amount of both horizontal displacements and coastal uplift increases with the decreasing viscosity of the weakest layer. Compared to the base model with uniform viscosity, deformation occurs in the weak layer of the asthenosphere in the depth-dependent viscosity

model. The flow magnitude increases at greater depth due to the weak layer while decreases at shallower depth (red arrow in Fig. 6c). The concentration of postseismic viscous strain at greater depth is also depicted by the difference between modeled strain and that of the base model (see strain difference in Fig. 6d).

We deployed depth-dependent viscosity in the oceanic mantle to investigate the effect of the oceanic asthenosphere on postseismic surface displacements. The thermal profile of the oceanic mantle was based on the half-space cooling model with a plate age of 120 Ma (Syracuse et al. 2010; See also Dhar et al. 2022). The thermal

model and rheological parameters are summarized in Additional file 1: Table S3. We investigated the effect of five oceanic mantle models using different activation volumes and water contents similar to the case of mantle wedge (Fig. 7a–b; see also Additional file 1: Table S3). Figure 7a compares the surface displacements of the models with various activation volumes and fixed water contents. With decreasing activation volume, the viscosity gradient of the oceanic asthenosphere decreases, which causes a larger displacement near the trench (cyan curve in Fig. 7a). Decreasing the activation volume also increases the thickness of the oceanic asthenosphere (Additional file 1: Fig. S2a) which largely affect the magnitude of the

coastal uplift (Fig. 7a). Similarly, Fig. 7b shows the surface displacements of the models with various water contents and the fixed activation volumes. Increasing the water content only reduces the viscosity of the oceanic asthenosphere which also strengthens the deformation near the trench (Fig. 7b). The weak oceanic asthenosphere (at a depth of ~100–180 km) controls the magnitude of the landward motion of the near-trench areas. In addition, it also controls the postseismic subsidence of the seafloor as well as the uplift in the areas close to the trench axis (Fig. 7). Although changes in either the activation volume or water content affect the surface deformation in similar ways, discrepancies can only be noticed in the

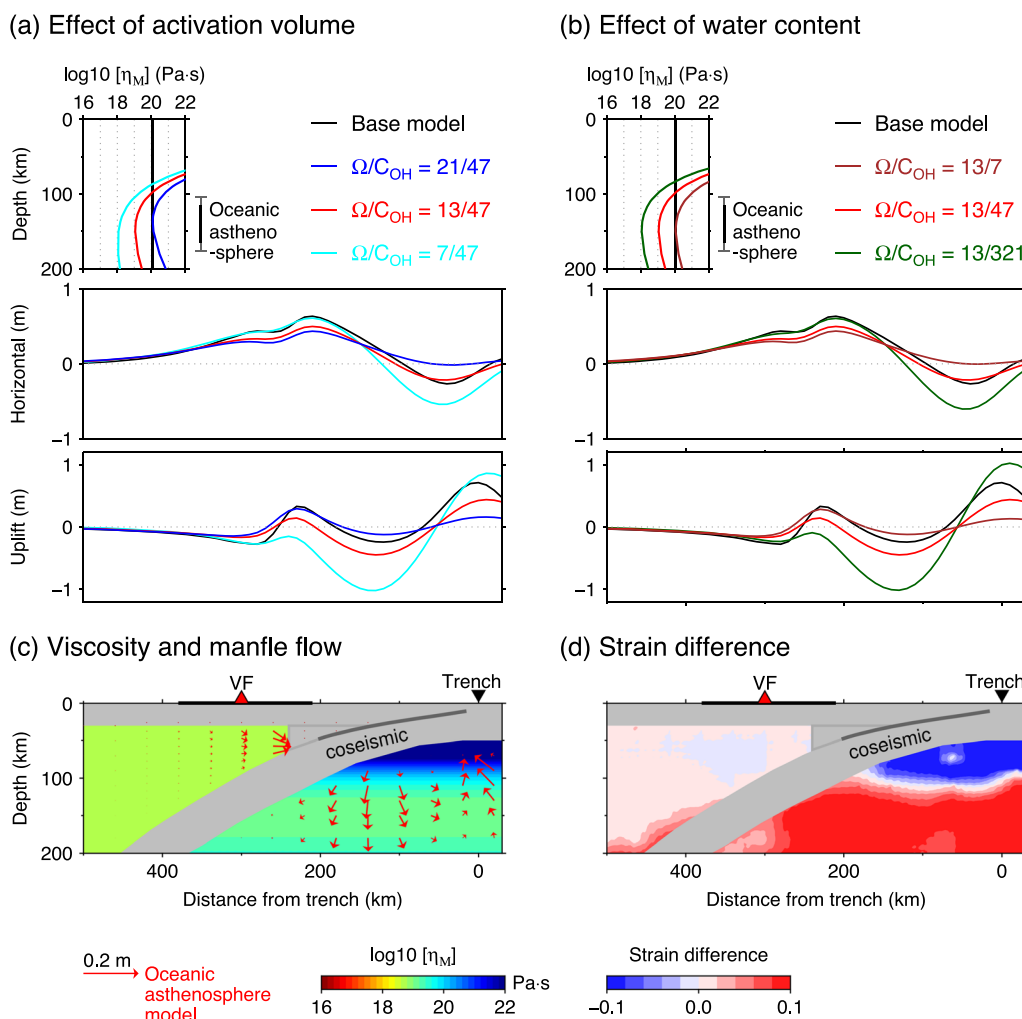


**Fig. 7** The effect of oceanic asthenosphere on the 3-year postseismic deformation **a** The surface displacement by the model with activation volume ( $\Omega$ ) vary as ~21, ~13, and ~7 cm<sup>3</sup>/mol while water content ( $C_{OH}$ ) was fixed to 47 ppm H/Si. The corresponding 1-D viscosity profiles are shown in top panel. **b** The surface displacement by the model with  $C_{OH}$  vary as ~7, ~47, ~321 ppm H/Si while  $\Omega$  was fixed to ~13 cm<sup>3</sup>/mol. The corresponding 1-D viscosity profiles are displayed in top panel. See model details in Additional file 1: Table S3. **c** The trench-normal profile shows the viscosity distribution and mantle flow pattern for the model with  $\Omega$ =~13 cm<sup>3</sup>/mol and  $C_{OH}$ =47 ppm H/Si are shown. **d** The distribution of strain difference corresponds to the model shown in (c). Strain difference = strain in depth-dependent model – strain in base model. All viscous strain (second invariant of the deviatoric strain tensor) is normalized by the coseismic strain

vertical deformation of the near-trench areas (see Fig. 7a, b). Similar to the mantle wedge, the weak oceanic asthenosphere allows significant mantle flow only at greater depth (red arrow in Fig. 7c). The strain distribution due to the depth-dependent models of oceanic mantle (relative to that of the base model) indicates the concentration of viscous strain at greater depth in the postseismic period (see strain difference in Fig. 7d).

#### 4.3 Low-viscosity zone beneath the volcanic front

We tested the effect of a localized low-viscosity zone (LVZ) beneath the volcanic front (300 km from the Japan Trench). The introduction of various LVZs in the base viscoelastic model causes a stronger local subsidence in the vertical displacements (as reported by the linear Burgers model of Muto et al. 2016). The presence of LVZ may influence the magnitude of horizontal displacements, but their pattern remains unchanged (Fig. 8a–d). The trench-normal dimension, the vertical dimension, and the depth of upper limit of the LVZs are, hereafter, referred as width (W), thickness (T), and top depth (D) of the LVZ, respectively (Fig. 8e). We investigated the surface deformation pattern using nine LVZ models with different W, T, D, and  $\eta_M$  (see also Additional file 1: Table S4). Figure 8a depicts the surface displacements by the model with different LVZ depths ( $D=30, 50, 70$  km) where other parameters are kept fixed. Similarly, Fig. 8b–d illustrates the effect of different LVZ thicknesses ( $T=20, 40, 60$  km), widths ( $W=40, 120, 200$  km) and Maxwell viscosities ( $\eta_M = 5.6 \times 10^{15}, 5.6 \times 10^{16}, 5.6 \times 10^{17}$  Pa·s), respectively. As noted, the local subsidence is highly sensitive to the depth of the LVZs; a shallower LVZ causes stronger subsidence (Fig. 8a). The increase in LVZ thickness (Fig. 8b) or decrease in its viscosity (Fig. 8d) not only adds more subsidence at the volcanic front but also causes uplift above the Pacific coast. The increase in LVZ width widens the areas of subsidence at the volcanic front and adds more uplift above the Pacific coast (Fig. 8c). For the LVZ model, flow vectors (red arrows in Fig. 8e) show a substantial increase in downward flow in the mantle beneath the volcanic front which explain the local subsidence in the vertical surface displacements. The strain difference of the LVZ model (Fig. 8f) illuminates the concentration of postseismic viscous strain beneath the volcanic front. Using a 2-D finite-element model, Yabe et al. (2015) also found a similar local strain anomaly associated with the LVZ beneath the Ou backbone range during the coseismic deformation of the 2011 Tohoku-oki earthquake.

Our investigation using simple 2-D models with various rheological structures leads to the conclusion that depth-dependent rheology and cold nose are responsible for the coastal uplift, whereas LVZ controls the subsidence

around the volcanic front, which altogether can qualitatively explain the postseismic observations after the 2011 Tohoku-oki earthquake. Apart from the cold nose, the presence of these three rheological units (depth-dependent viscosity, deeper LVZ, and oceanic asthenosphere) is required to produce the first-order pattern of vertical deformation while their thicknesses, depths, and viscosities control the amplitude of deformation.

## 5 Rheological heterogeneities constrained by geodetic observations

### 5.1 Models of postseismic deformation in the last decade

We reviewed 22 postseismic models developed in the last decade and summarized the inferred rheology in Table 1. Numerous models have used uniform viscosity for the entire mantle wedge and oceanic mantle (Sun et al. 2014; Diao et al. 2014; Hu et al. 2014, 2016; Iinuma et al. 2016; Suito 2017; Fukuda and Johnson 2021; Luo and Wang 2021). On the other hand, several studies have used spatially varied heterogeneous viscosity models (Freed et al. 2017; Suito 2017; Agata et al. 2019; Muto et al. 2016, 2019; Dhar et al. 2022) to simulate postseismic crustal deformation. Notably, power-law or depth-dependent rheology can influence substantially on coastal uplift (as discussed in Sect. 4), which can also be controlled by deeper AS (Muto et al. 2019; Dhar et al. 2022; Luo and Wang 2022). Thus, depth-dependent rheology can share potential trade-off with heterogeneously distributed AS on the plate boundary fault. Regardless of the uniform or heterogeneous viscosity structures in the mantle wedge, all postseismic models simulated the seaward horizontal motion of inland GNSS stations and landward motion of seafloor GNSS-A stations. Several models have deployed biviscous Burgers rheology to explain postseismic deformation (Sun et al. 2014; Sun and Wang 2015; Wang et al. 2018; Agata et al. 2019; Muto et al. 2016, 2019; Fukuda and Johnson 2021; Dhar et al. 2022). Only a few models explained cumulative surface displacements using linear Maxwell rheology (Diao et al. 2014; Yamagiwa et al. 2015; Freed et al. 2017; Suito 2017).

For the oceanic asthenosphere, most biviscous Burgers rheology models estimate the transient viscosity on the order of  $\sim 2\text{--}4 \times 10^{18}$  Pa·s (Sun et al. 2014; Sun and Wang 2015; Iinuma et al. 2016; Fukuda and Johnson 2021). The Maxwell model of Suito (2017) and Freed et al. (2017) employed a viscosity of  $\sim 1 \times 10^{17}\text{--}1 \times 10^{18}$  Pa·s for the oceanic asthenosphere. Interestingly, Yamagiwa et al. (2015) used a layered earth model and estimated a higher viscosity of  $\sim 9 \times 10^{18}$  Pa·s than the above-mentioned models. The reason for this higher viscosity is probably the absence of a subducting Pacific slab in their model as pointed out by Wang et al. (2018). The thickness of the Pacific slab has a larger influence on the estimated

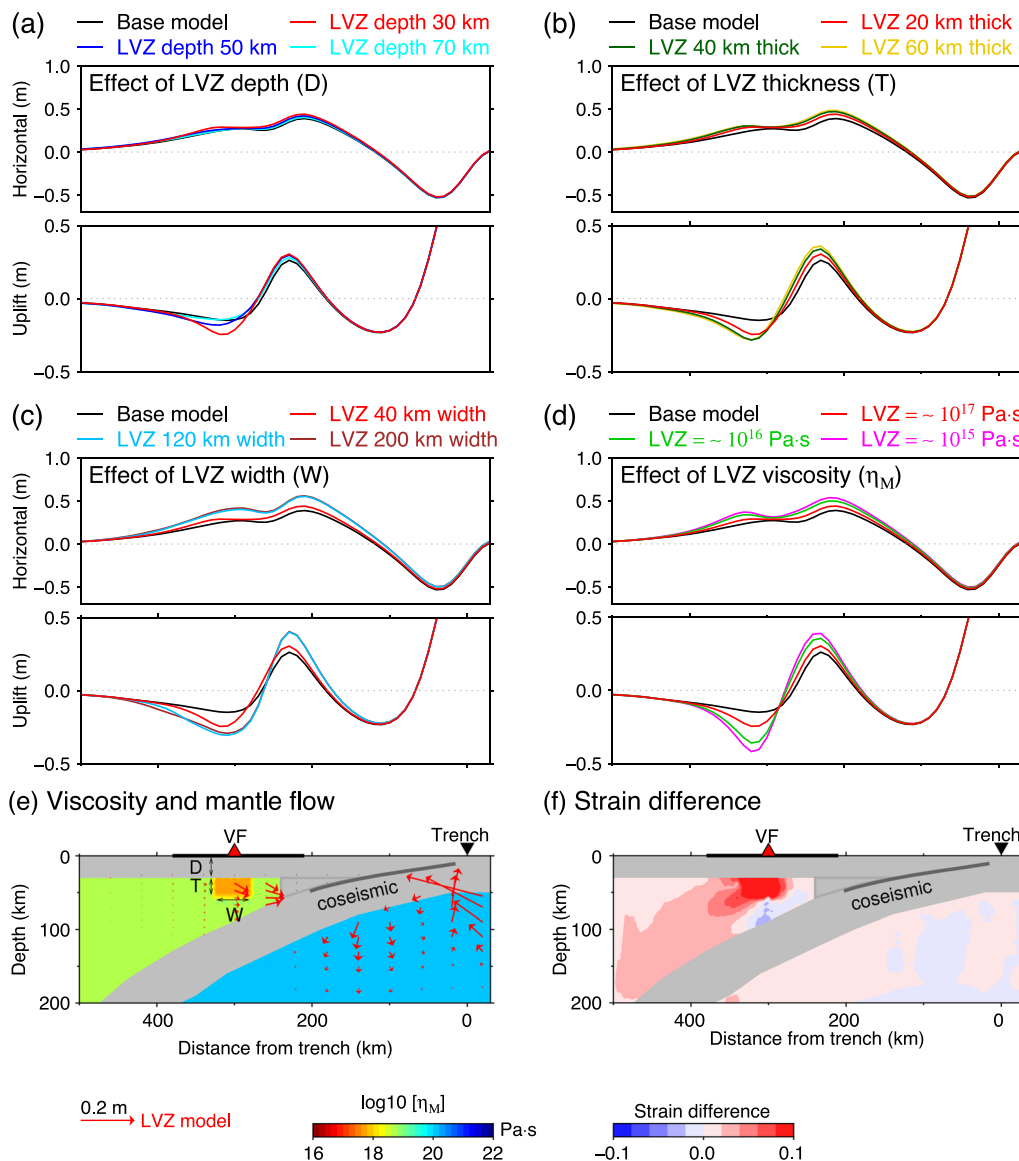


**Fig. 8** The effect of LVZ on the 3-year postseismic deformation **a** the surface displacement by the models with top depth  $D$  at 30 km, 50 km, and 70 km, while  $T=20$  km,  $W=40$  km, and  $\eta_M=5.6 \times 10^{17}$  Pa·s. **b** The surface displacement by the models with thickness  $T$  at 20 km, 40 km, and 60 km, while  $D=30$  km,  $W=40$  km, and  $\eta_M=5.6 \times 10^{17}$  Pa·s. **c** The surface displacement by the models with width  $W$  at 40 km, 120 km, and 200 km, while  $D=30$  km,  $T=20$  km, and  $\eta_M=5.6 \times 10^{17}$  Pa·s. **d** The surface displacement by the models with Maxwell viscosity  $\eta_M$  at  $5.6 \times 10^{17}$  Pa·s,  $5.6 \times 10^{16}$  Pa·s,  $5.6 \times 10^{15}$  Pa·s, while  $D=30$  km,  $T=20$  km, and  $W=40$  km. **e** The trench-normal profile depicts the viscosity distribution and mantle flow pattern for the model with  $D=30$  km,  $T=20$  km,  $W=40$  km, and  $\eta_M=5.6 \times 10^{17}$  Pa·s. **f** The distribution of strain difference corresponds to the model shown in (e). Strain difference = strain in LVZ model – strain in base model. All viscous strain (second invariant of the deviatoric strain tensor) is normalized by the coseismic strain

viscosity of oceanic mantle (Miyashita 1987; Sun and Wang 2015). The elastic subducting slab decelerates viscoelastic flow, leading to a reduction in landward motion above the main rupture area (Sun and Wang 2015; Wang et al. 2018; Li and Chen 2022). The thickness of the Pacific slab is estimated to be around  $\sim 80$ – $100$  km, as inferred by high-resolution seismic tomography, receiver-function analysis, and paleo-age data of the ancient

seafloor (e.g., Kawakatsu et al. 2009; Zhao et al. 2012; Liu and Zhao 2016; Liu et al. 2017). Most postseismic models consider various thicknesses of the Pacific slab, ranging from 25 to 100 km (e.g., Sun et al. 2014; Freed et al. 2017; Agata et al. 2019). To fit the same geodetic observation dataset, a model with a thinner subducting plate requires a higher viscosity, whereas the model with a thicker subducting plate requires a lower viscosity.

Furthermore, several studies (Hu et al. 2014; Iinuma et al. 2016; Freed et al. 2017) have argued that postseismic crustal deformation may be influenced by the subduction of the Philippine Sea Plate, especially in the southern part of NE Japan. Freed et al. (2017) illustrated that the subducting Philippine Sea Plate may extend only ~100 km depth beneath the Kanto region. Analysis of the seismic velocity profile beneath the Kanto and Chubu regions suggests that the Philippine Sea Plate of ~60-km thickness terminates between depth of ~90 and 200 km on the Pacific Plate (Nakajima and Hasegawa 2007; Nakajima et al. 2009). Hu et al. (2016) inferred the viscosity of the asthenosphere beneath the Philippine Sea Plate to be  $\sim 10^{18}$  Pa·s, suitable for producing VR affecting the onshore and offshore crustal displacements in southern NE Japan. Nevertheless, more studies are needed to resolve the contribution of the Philippine Sea Plate’s asthenosphere to the postseismic deformation of NE Japan.

Although we introduce various postseismic models with different rheological characteristics in the next chapter, reader should note that a direct comparison of the model parameters listed in Table 1 is not always possible. Each postseismic model was tailored to different modeling strategies, observational datasets (time windows and spatial coverage), and study-specific objectives. Due to the inherent trade-offs between different rheological units (as discussed above), the adaptation of the properties of rheological units varies widely throughout the published postseismic models. Moreover, most postseismic models have primarily focused on fewer rheological units aiming to explain the first-order characteristics

of the postseismic deformation (Sun et al. 2014; Sun and Wang 2015; Wang et al. 2018; Fukuda and Johnson 2021), whereas the later studies have targeted fine details of rheological heterogeneity with more complex rheology and viscosity structures (Muto et al. 2016, 2019; Luo and Wang 2021; Dhar et al. 2022).

### 5.2 Depth-dependent rheological model

As shown in our 2-D model with depth-dependent viscosity (see Sect. 4.2), viscoelastic flow occurs in weaker part of the lower crust and upper mantle in response to the coseismic stress perturbation (Freed et al. 2017; Suito 2017; Riva and Govers 2009). A change in the pattern of viscous stratification in any viscosity model can affect the modeled surface deformation in time and space (Freed and Bürgmann 2004; Riva and Govers 2009; Yamasaki and Houseman 2012; Freed et al. 2017; Suito 2017). Here, we review several different models described by Suito (2017) and Freed et al. (2017) to understand the role of depth-dependent rheology in surface deformation patterns. Figure 9 shows the surface deformation produced by the four pure viscoelastic models of Suito (2017). Model 1 shows a uniform viscosity of  $2 \times 10^{18}$  Pa·s for both mantle wedge and oceanic mantle. Model 2 shows a uniform viscosity of  $2 \times 10^{18}$  Pa·s for the mantle wedge and  $1 \times 10^{19}$  Pa·s for the oceanic mantle. Model 3 introduces a low-viscosity ( $1 \times 10^{18}$  Pa·s) thin layer of lithosphere–asthenosphere boundary (LAB) beneath the Pacific slab. Model 4 incorporates depth-dependent viscosity stratification in the mantle wedge, where the lowest viscosity of  $1 \times 10^{18}$  Pa·s was located at a depth of ~200–300 km. In response to coseismic stress perturbations, the mantle

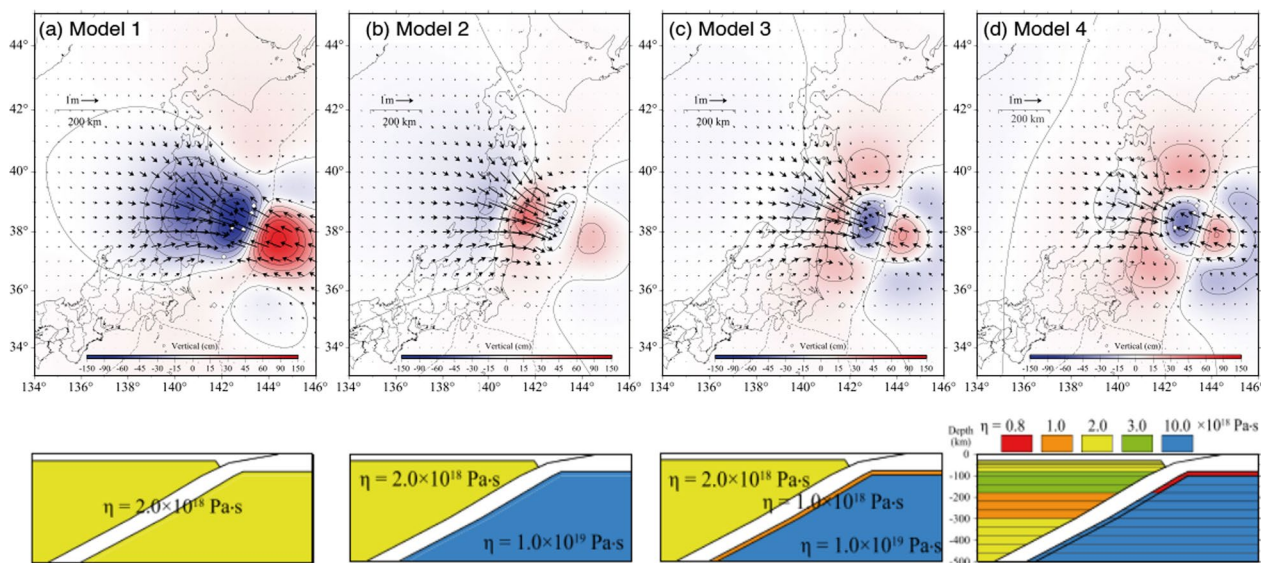


**Fig. 9** The effect of depth-dependent rheology in the postseismic crustal deformation (after Suito 2017)

wedge produces a trenchward motion, whereas the oceanic mantle produces a landward motion. Models 1–3, using almost uniform viscosity, reproduce similar surface deformation patterns to our simple 2-D models (Fig. 4a) and show stronger uplift at the Pacific coast, subsidence in western Japan, and subsidence at the seafloor near the trench. When depth-dependent viscosity is introduced in the mantle wedge (Model 4), a stronger contrast in the lateral deformation pattern appears, which is consistent with the observed geodetic deformations (stronger subsidence in the central region).

Depth-dependent viscosity can considerably improve the spatial distribution of the calculated residuals between the observed and modeled displacements (Fig. 10). For example, the model with depth-dependent

viscosity (Model 9 in Freed et al. 2017) produces misfits of almost half that of the model with uniform viscosity (Model 11) in the horizontal and vertical components (Table 1 in Freed et al. 2017). In particular, the best-fit viscoelastic structure with depth-dependent viscosity in Freed et al. (2017) successfully explained the geodetic observation of the central Tohoku district, which is the region closest to the main rupture area (Fig. 10). However, depth-dependent viscosity alone is not sufficient to explain the broader deformation pattern. The combined model of Freed et al. (2017) explained the observations in the Kanto region and the northern part of Iwate Prefecture by AS components using kinematic inversion. Furthermore, the depth-dependent viscosity in Suito (2017) and Freed et al. (2017) may not have significant effects

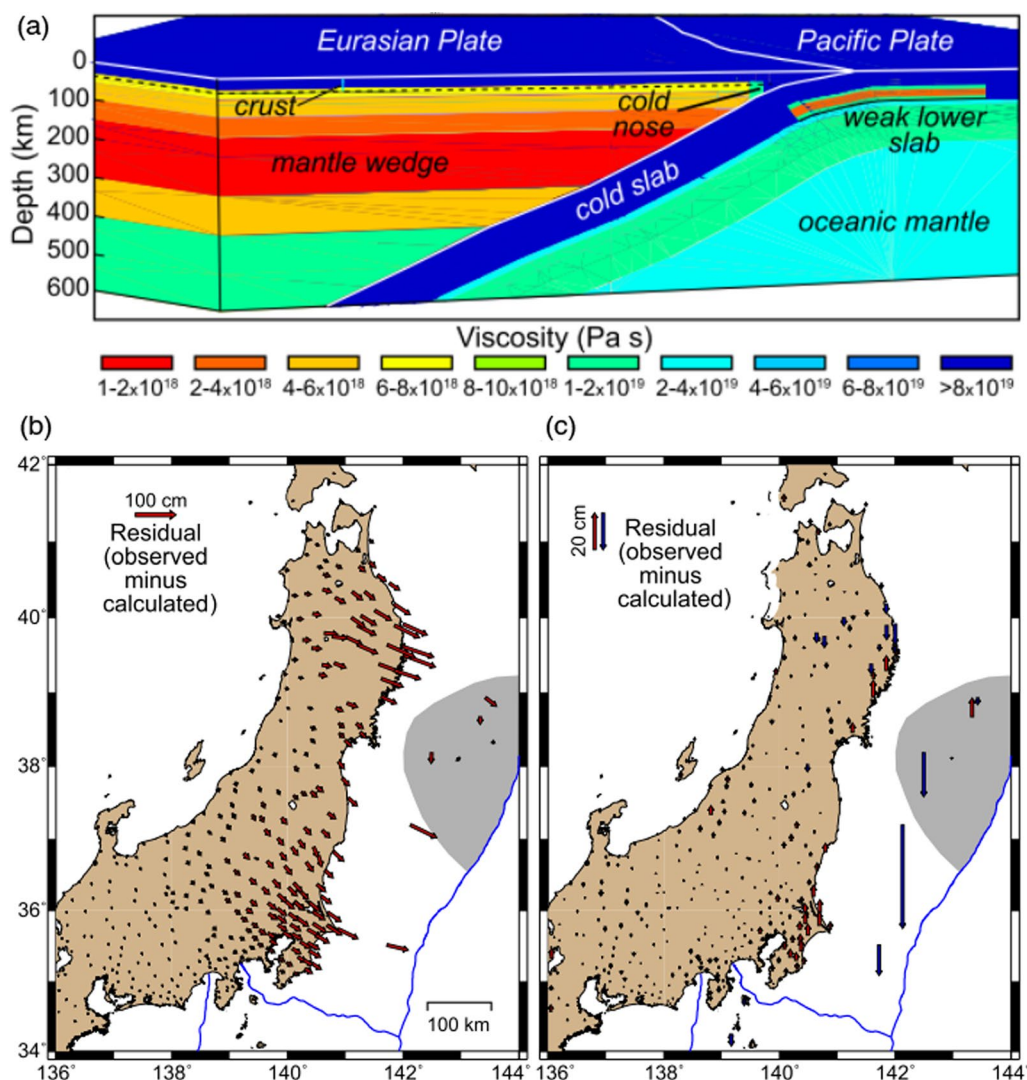


**Fig. 10** a Depth-dependent rheology model and calculated residuals (= observed – modeled by VR) in **b** horizontal and **c** vertical direction (after Freed et al. 2017)



on coastal uplift (see results of model 4 of Suito 2017), in contrast to the result of our depth-dependent viscosity model (Fig. 6). This is likely due to the deeper depth of the weak layer ( $\sim 150\text{--}300$  km) in their model with Maxwell rheology, in contrast to the shallower depth of  $\sim 80\text{--}120$  km in our model (Fig. 6a-b). These Maxwell models usually explain surface displacement in cumulative but not their time-series.

### 5.3 Low-viscosity zone in sub-arc mantle wedge

The coseismic rupture of the 2011 Tohoku-oki earthquake caused large-scale subsidence around the Pacific coast of NE Japan, up to  $\sim 1.2$  m observed near the large coseismic slip zone such as the Ishinomaki area. In addition, Takada and Fukushima (2013) reported small-scale subsidence near Quaternary volcanoes during the 2011 Tohoku-oki earthquake. The regions near Mt. Akita-koma, Mt. Kurikoma, Mt. Zao, Mt. Azuma, and Mt. Nasu show localized subsidence of 5–15 cm in the shape of elongated elliptical depressions with horizontal dimensions up to 15–20 km. The subsided regions coincide with the regions of high heat flow, hot thermal water (Tanaka et al. 2004), and late Cenozoic calderas (Yoshida 2001), indicating the presence of magmatic bodies beneath these areas. The thermally weakened rock beneath these regions accommodates dilation in response to coseismic stress perturbations which may cause such subsidence.

Based on GEONET observations during the post-seismic period, Hu et al. (2014) explained the vertical observation pattern. As shown by our simple 2-D model (Fig. 8), the presence of a localized weak zone in the lower crust ( $\sim 40$  km wide) reproduces subsidence at the volcanic front and uplift along the Pacific coast. They demonstrated that the weak zone may have a deeper root, up to  $\sim 30$  km depth, to produce large-scale subsidence ( $\sim 100$  km; Hu et al. 2014) during the postseismic period. Muto et al. (2019) and Dhar et al. (2022) incorporated a low-viscosity backarc mantle into their models (Fig. 11a). The wider and deeper roots of the LVZ may correlate with the upwelling mantle flow associated with slab dehydration and corner flow in the Japan mantle wedge illuminated by seismological observations (e.g., Zhao et al. 1994; Iwamori and Zhao 2000; Hasegawa et al. 2005, 2009; Huang et al. 2011; Tong et al. 2012; Zhao 2012; Nakajima et al. 2013). Previous seismic tomography has revealed a low-velocity zone in the central part of NE Japan, which may extend to the eastern margin of the Japan Sea (e.g., Zhao et al. 1994; Iwamori and Zhao 2000; Hasegawa et al. 2005, 2009; Huang et al. 2011; Tong et al. 2012; Zhao 2012). By analyzing the seismic attenuation over NE Japan, Nakajima et al. (2013) recognized this upwelling mantle flow as an inclined high-attenuation zone beneath the backarc mantle wedge

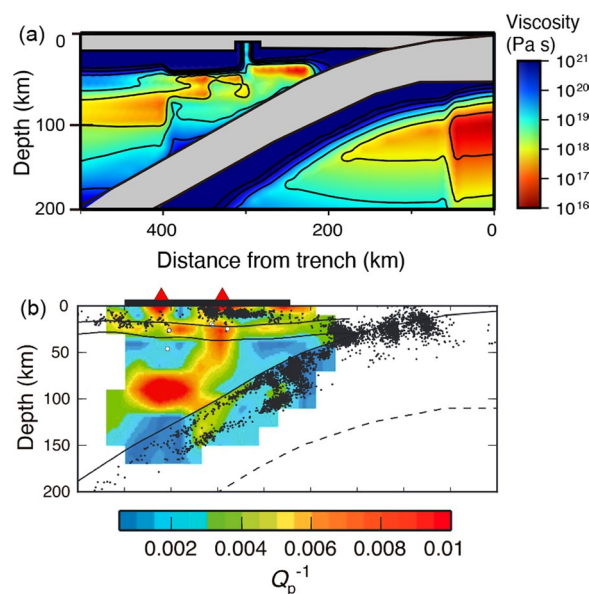


**Fig. 11** **a** The heterogeneous rheology in the 2-D postseismic model of Muto et al. (2019). **b** The seismic P-wave attenuation profile across the Miyagi-Yamagata transect from Nakajima et al. (2013)

(Fig. 11b). The partial melt produced by the dehydration of the Pacific slab ( $< 120$  km) may attribute to this high-attenuation zone. By comparing seismic attenuation with velocity structure, Nakajima et al. (2013) also concluded an along-arc variation of partial melts that cluster beneath Quaternary volcanoes of central NE Japan. The along-arc variation in the lower crustal rheology is also reflected in the heat flow and thermal gradient observations along the volcanic front, where a local anomaly is observed in the vicinity of Quaternary volcanoes (Tanaka et al. 2004; Matsumoto et al. 2022). Based on the spatial variation in the thermal gradient, Tamura et al. (2002) referred to a hot mantle finger model for the volcanic front of NE Japan.

The shape of such weak zones was later refined using  $\sim 9$  months of observations (Fig. 12a) from the THK network (Muto et al. 2016). Muto et al. (2016) identified a small-scale LVZ beneath Mt. Naruko in the Miyagi region (Fig. 12b). The protrusion of the LVZ can be as shallow as  $\sim 5$  km from the surface. The width of this shallow LVZ can be  $\sim 10$  km to reproduce small-scale surface subsidence (Muto et al. 2016). The geometry of the LVZ inferred from geodetic observations is identical to the observations of low resistivity (Fig. 12c; Ogawa et al. 2014) and low seismic velocity (Fig. 12d; Okada et al. 2014) beneath this region. Thus, the LVZ can be correlated with the magma chamber beneath the volcanoes (Okada et al. 2014). The steady-state

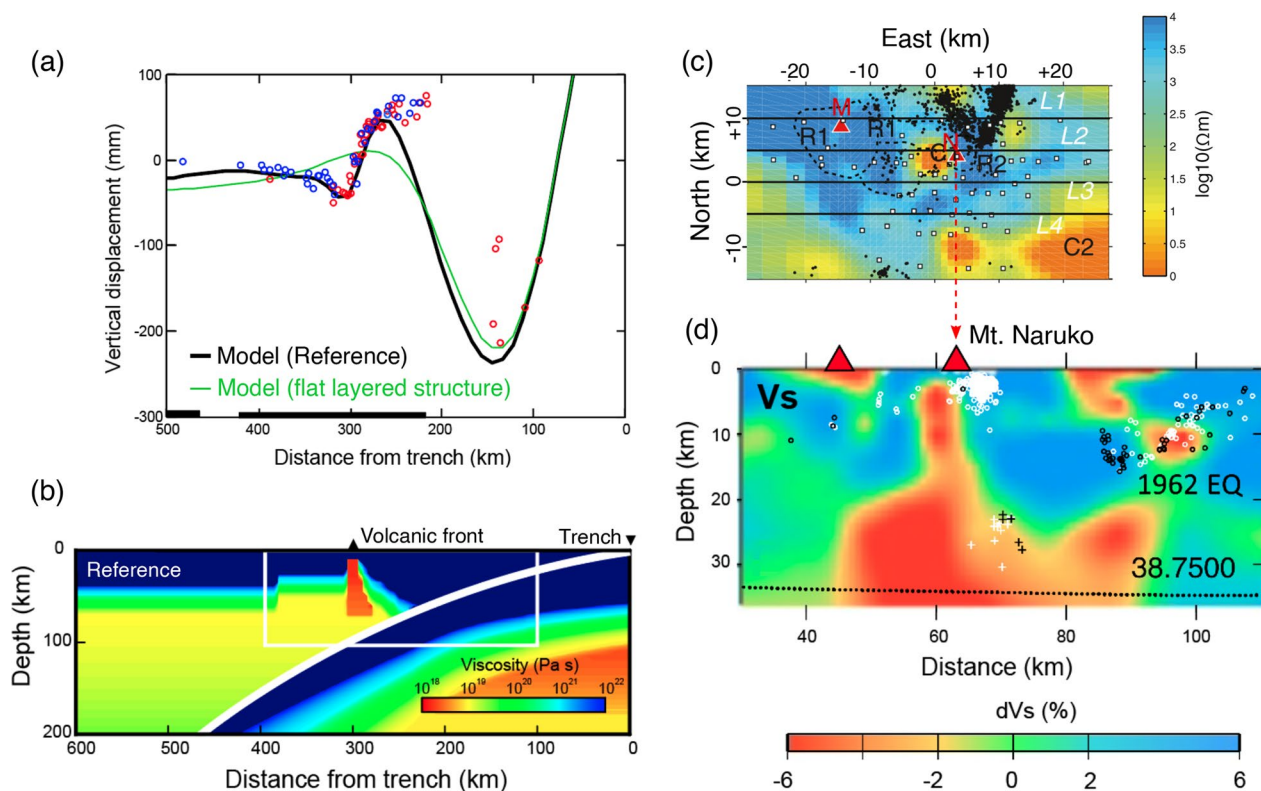


**Fig. 12** **a** Two-dimensional projection of observed and modeled displacements along Miyagi-Yamagata area (Muto et al. 2016). The blue and red points denote GNSS observations from GEONET and Tohoku university network, respectively. **b** Two-dimensional viscosity structure across Mt. Naruko region (after Muto et al. 2016). **c** Map view of resistivity distribution (at 5 km depth) around Mt. Naruko by magnetotelluric survey (after Ogawa et al. 2014). **d** S-wave tomography for the same transects (after Okada et al. 2014)

viscosity of the LVZ can be as low as  $10^{16}$  Pa·s (Muto et al. 2016), which is consistent with that of silica-rich rhyolitic magma (Ban et al. 2005). Approximately 2 years following the mainshock, the subsidence at the GNSS stations (e.g., Naruko stations in Fig. 2F in Muto et al. 2019) in the volcanic region is reported to have ceased, implying almost full relaxation of coseismic stress (Muto et al. 2019; Dhar et al. 2022). The shorter relaxation timescale and larger response immediately after the earthquake indicate lower viscosity than that of the surrounding mantle. Several studies have incorporated the shallow LVZ and backarc mantle upwelling flow in their viscoelastic structure to simulate geodetic observations in both horizontal and vertical directions (Muto et al. 2016, 2019; Dhar et al. 2022).

#### 5.4 Oceanic asthenosphere

Seismic and geodetic networks deployed on the seafloor play pivotal roles in deciphering the rheology of the subducting slab and oceanic mantle. Several studies

have explored the rheology of oceanic asthenosphere to explain the postseismic landward movement of seafloor GNSS stations (Hu et al. 2016; Freed et al. 2017; Agata et al. 2019; see Masuti et al. 2016 for Sumatra). According to receiver-function analysis that illuminates a sharp change in rheological properties at the lithosphere–asthenosphere boundary (LAB, Kawakatsu et al. 2009), most linear viscoelastic models incorporated a thin low-viscous layer along the LAB in the upper mantle beneath the Pacific slab around at a depth of 80–90 km (Sun et al. 2014; Suito 2017; 40–80 km in Freed et al. 2017). The introduction of the LAB layer reduces the ratio of vertical to horizontal displacements at the seafloor and reproduces results more consistent with the observations.

On the other hand, by deploying power-law Burgers rheology, Agata et al. (2019) pointed out that the LAB may not be a permanent low-viscous part in the oceanic mantle but may be due to the transient reduction in effective viscosity in response to coseismic stress perturbation (Fig. 13a–b). Over time, the viscosity increased and returned to the pre-earthquake steady-state viscosity (Fig. 13b–c). The location of the rapid decrease in the

effective viscosity (depth of ~100–180 km) is controlled by the coseismic stress changes and stress-dependent viscosity (Eq. 2 and Fig. 8), and consistent with the location of the reduced seismic velocity beneath the Pacific Ocean (Kawakatsu et al. 2009). This depth-dependent seismic anomaly can be explained by the presence of partial melt (Kawakatsu et al. 2009; Hirschmann 2010) or fluids (Karato and Jung 1998; Karato 2012). The robustness of any conclusion requires further study from a mineral-physics perspective and more observational constraints.

### 5.5 Cold nose

The cold nose is referred to as the stagnant part of the forearc mantle wedge which does not partake in mantle-wedge corner flow (Furukawa 1993; Wada and Wang 2009). Owing to the cold and high viscosity, the cold nose is devoid of any viscous flow and, thus, decoupled from the subducting slab (Fig. 14a, Uchida et al. 2020; Luo and Wang 2021; see also Fig. 4a). Most often, postseismic models consider the cold nose as either an elastic (Sun et al. 2014; Hu et al. 2014, 2016; Agata et al. 2019; Fukuda and Johnson 2021; Luo and Wang 2021; Fig. 4a) or a high viscous (Muto et al. 2016, 2019; Freed et al. 2017; Dhar et al. 2022) part of the mantle wedge. Recently, an analysis of a newly deployed seafloor seismic network (S-net) revealed that a cold nose displays no or weaker seismic anisotropy (Uchida et al. 2020). In contrast, the backarc mantle shows distinct anisotropy that can be interpreted

by the lattice-preferred orientation of olivine formed in the backarc mantle flow (Okada et al. 1995; Nakajima and Hasegawa 2006; Nakajima et al. 2006; Huang et al. 2011). Therefore, the cold nose provides a sharp rheological contrast between the high viscous or elastic part of the forearc and rest of the mantle wedge. Hereafter, we refer to the western edge location of the cold nose as cold-nose edge (CNE, Luo and Wang 2021).

Luo and Wang (2021) pointed out that the CNE may also play an important role in creating a first-order pattern of ground uplift in the postseismic period of great subduction zone earthquakes (Fig. 14b). GNSS observations in subduction zones such as Chile, Sumatra, and Japan have recorded a substantial crustal uplift above the forearc in recent decades (Luo and Wang 2021). Several studies have concluded that VR contributes to forearc uplift during the transient postseismic period (Freed et al. 2017; Muto et al. 2016, 2019; Luo and Wang 2021; Dhar et al. 2022). Luo and Wang (2021) demonstrated that the CNE deflects viscoelastic flow upward during the postseismic deformation of megathrust events. The upward deflection of the coseismically triggered viscoelastic flow causes a crustal uplift along the CNE location. The difference between the vertical uplift produced by the models with and without a cold nose is also illustrated in the pure viscoelastic model of Muto et al. (2016; see also our 2-D model in Fig. 4a).

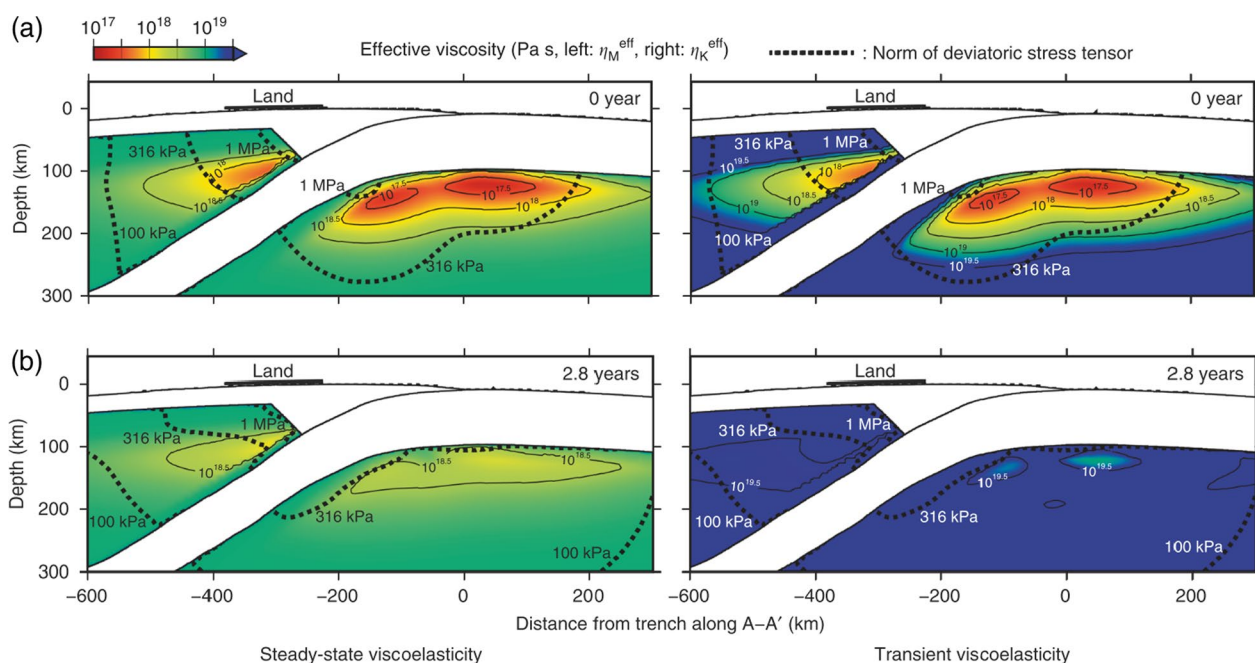


**Fig. 13** The effective viscosity of steady-state (left) and transient creep (right) estimated by Agata et al. (2019). **a** 0 year, **b** 2.8 years after the earthquake. The profile is along the Miyagi-Yamagata areas

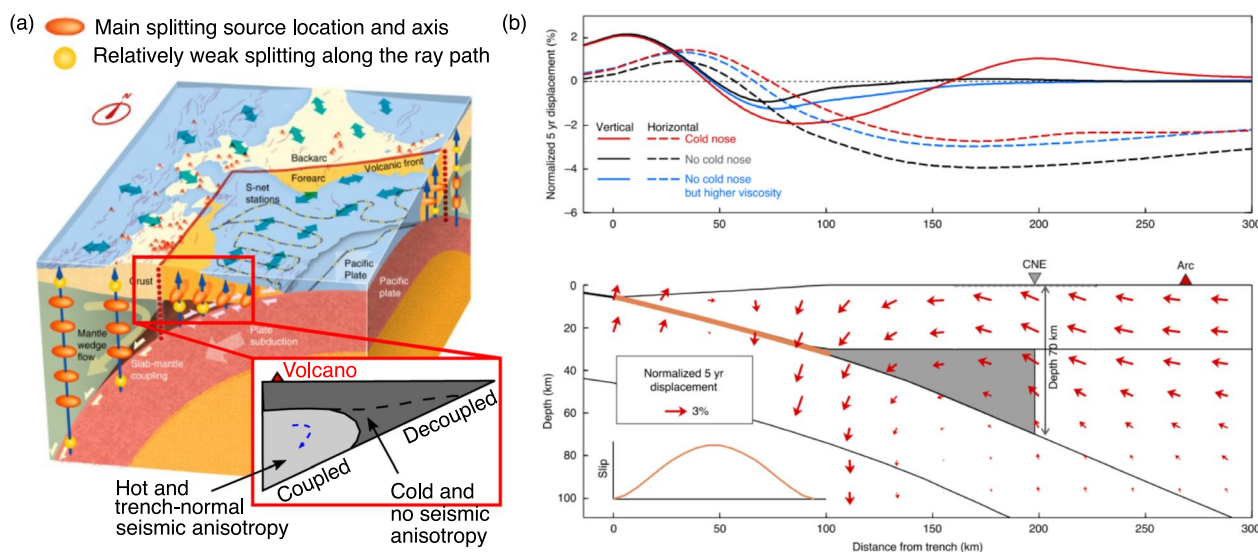


**Fig. 14** **a** Seismic anisotropy and thermal contrast in the forearc mantle (after Uchida et al. 2020). **b** The effect of cold nose in the surface deformation during 5 years of postseismic period (after Luo and Wang 2021)

The cold nose in the viscoelastic models influences the viscosity of the mantle wedge. The presence of a cold nose reduces the estimated viscosity of the mantle wedge compared with the model without a cold nose (Luo and Wang 2021). For example, Hu et al. (2014, 2016) estimated a steady-state viscosity of approximately  $1\text{--}3 \times 10^{19}$  Pa·s without incorporating a cold nose. However, the postseismic models of Sun et al. (2014) inferred a steady-state viscosity of  $1.8 \times 10^{18}$  Pa·s by incorporating a cold nose into their model. All these models used the same linear Burgers rheology with the same rigidity modulus of 64 GPa despite different elastic continental-plate thicknesses. Although a thick elastic plate causes a reduction in viscosity, as reviewed by Wang et al. (2018), the difference in plate thickness does not explain the lower estimates of viscosity in Sun et al. (2014). As noted, Hu et al. (2014, 2016) employed a  $\sim 40$ -km-thick continental plate compared to 25 km of Sun et al. (2014). As investigated by Luo and Wang (2022), terrestrial surface deformation (both horizontal and vertical) is only sensitive to the rheology of mantle wedge. Therefore, one of the possible reasons for the lower estimates for mantle wedge viscosity is the presence of a cold nose. Similar to Sun et al. (2014), the lower value of steady-state viscosity on the order of  $10^{17}\text{--}10^{18}$  Pa·s is also estimated by most postseismic models that incorporated a high viscous or elastic cold nose (Freed et al. 2017; Suito 2017; Muto et al. 2016, 2019; Fukuda and Johnson 2021; Luo and Wang 2021; Dhar et al. 2022).

Although seismic observations have illuminated the ubiquitous nature of the cold nose along NE Japan (Uchida et al. 2020), previous postseismic observations

have illuminated the location of CNE to be 200–300 km from Japan-trench axis (Freed et al. 2017; Muto et al. 2016, 2019; Agata et al. 2019; Luo and Wang 2021; Dhar et al. 2022). Dense GNSS observations deployed by Tohoku University along the Miyagi and Fukushima prefectures show the along-arc variations in the location of CNE (Dhar et al. 2022). Dhar et al. (2022) inferred a narrower cold-nose geometry for the Miyagi transect and a wider cold-nose geometry for the Fukushima transect (Fig. 15). This indicates that the CNE extends more toward land in the Fukushima area than in the Miyagi area. The along-arc rheological variation can be correlated to other geophysical observations, including the deepening of the D90 depth (above which 90% inland earthquake occurs, Omuralieva et al. 2012) and locally depressed geothermal gradient above Fukushima prefecture (Tanaka et al. 2004; Matsumoto et al. 2022). The deepening of the D90 depth in the Fukushima prefecture indicates a deeper brittle-ductile transition compared with that of the Miyagi forearc and is consistent with the colder Fukushima forearc.

## 6 Challenges and future issues

### 6.1 Relative contribution of viscoelastic relaxation and afterslip

Although we have reviewed many postseismic models of combined VR and AS (Table 1), terrestrial observations following the 2011 Tohoku-oki earthquake were also well explained by pure AS models (e.g., Ozawa et al. 2012), similar to those developed for the Chile or Sumatra subduction zones (Pritchard and Simons 2006; Hsu et al. 2006). These models only considering AS are

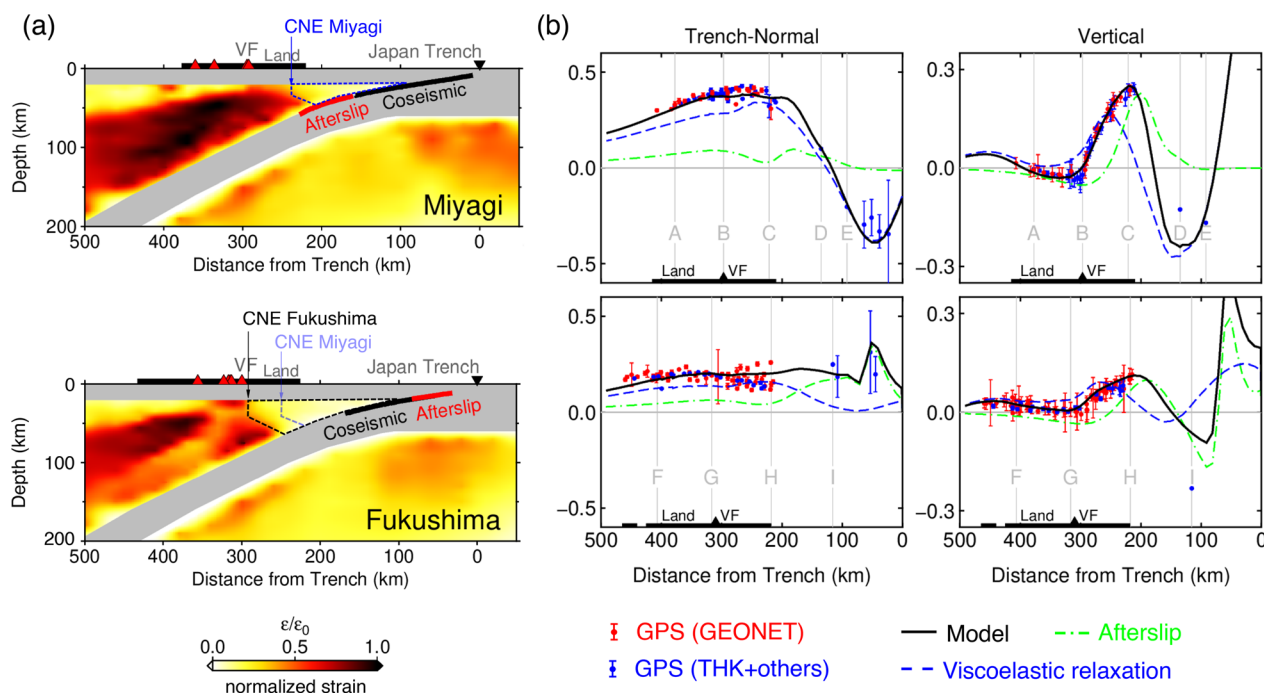


**Fig. 15** **a** Total strain by viscous flow during  $\sim 5$  years of postseismic deformation along the Miyagi-Yamagata region and the Fukushima-Niigata region (after Dhar et al. 2022). **b** The two-dimensional projection of modeled displacements from September 2012 to May 2016 along the Miyagi-Yamagata region and Fukushima-Niigata region

consistent with the previous consensus that AS dominates short-term, near-field crustal deformation, whereas VR dominates long-term deformation after the earthquake. However, this consensus was challenged by the remarkable discovery of landward motion of the seafloor which provided unambiguous evidence of VR dominance in short-term postseismic deformation (Sun et al. 2014; Watanabe et al. 2014). Since then, many postseismic models have combined VR and AS to explain horizontal postseismic deformation following the 2011 Tohoku-oki earthquake (Diao et al. 2014; Shirzaei et al. 2014; Sun et al. 2014; Sun and Wang 2015; Yamagiwa et al. 2015; Hu et al. 2016; Freed et al. 2017; Suito 2017; Wang et al. 2018; Agata et al. 2019; Muto et al. 2019; Fukuda and Johnson 2021; Dhar et al. 2022). Most postseismic models suggest that VR dominates the horizontal motion in the central Tohoku district where the coseismic stress change was significant. The larger contribution of VR to short-term inland postseismic deformation contradicts the older consensus on the domination of AS.

The relative contributions of VR and AS inferred from a postseismic study strongly depend on the nature of the deployed viscoelastic models. The modeled VR and AS components of crustal displacements usually share a trade-off because both deformation sources produce similar surface deformations following megathrust earthquakes (Hu et al. 2016; Freed et al. 2017; Masuti et al.

2016; Luo and Wang 2022). The model assumption on the rheological heterogeneities and governing constitutive laws also affects the AS distribution on the plate boundary fault; however, the trade-off between these AS and each mantle heterogeneity is still poorly understood. Several studies calculated their VR components by deploying a pure viscoelastic model, inverting the remaining residuals to estimate the AS components (kinematic inversion in Iinuma et al. 2016; Freed et al. 2017; Sun et al. 2014; Sun and Wang 2015; Shirzaei et al. 2014; Wang et al. 2018). In other words, AS components are complementary to the modeled VR components which originate from a specific viscoelastic structure. For example, Wang et al. (2018) argued that the presence of a subducting slab may affect the estimation of deep AS directly downdip of the main rupture area (see also Li and Chen 2022).

Recently, several postseismic studies deployed stress-dependent deformation models based on experimental rock physics (Barbot 2020; Agata et al. 2019; Muto et al. 2019; Fukuda and Johnson 2021; Dhar et al. 2022) and simultaneously simulated the VR and AS components of postseismic surface displacements. Statistical analysis indicated the possibility of trade-offs among the deformation parameters related to the VR and AS components (Fukuda and Johnson 2021; Dhar et al. 2022). Some studies may infer strong (Masuti et al. 2016) and modest (Dhar et al. 2022) VR-AS trade-offs, whereas others

may not (Fukuda and Johnson 2021). This is probably due to the employment of different modeling strategies and methods of parameter-space search; however, further analysis is required in this regard. Moreover, these models highlight the importance of mechanical coupling between AS and VR where the two deformation sources influence each other (Agata et al. 2019; Muto et al. 2019). Based on a two-dimensional mechanical model, Muto et al. (2019) demonstrated that the effect of coupling on the surface deformation was small or negligible in the early phase of the postseismic deformation. However, this coupling becomes more pronounced over time and affects the long-term studies of the postseismic deformation, such as the recovery of plate coupling and coseismically subsided coastal areas. Furthermore, as indicated by previous studies, both VR and AS can have a local influence on postseismic deformation (e.g., Luo and Wang 2022; Muto et al. 2016). Therefore, an accurate estimation of their local influences may be crucial for estimating the recovery of plate coupling (i.e., backslip that produces the opposite pattern to the afterslip). In the coming decade, incorporating backslip into postseismic models may be more relevant as significant plate coupling seems to appear in the recent GNSS dataset (Watanabe et al. 2021).

### 6.2 Role of rheological heterogeneity for earthquake cycle

The decade-long leveling dataset and GNSS observations before the 2011 Tohoku-oki earthquake indicated a rapid interseismic subsidence of approximately 5 mm/yr over the last decade (Nishimura 2014). This significant subsidence has created a paradox as the geological uplift rate of NE Japan measured to be approximately 0.1–0.5 mm/yr by the analysis of Quaternary marine terraces (Ota and Omura 1991). Several interseismic models suggest that rapid subsidence only takes place in the last stage of the interseismic period where postseismic uplift is converted to subsidence a decade before the occurrence of the M9 earthquake (e.g., Nishimura 2014). See Shibasaki (2023) for the detail of the interseismic subsidence by Sasajima et al. (2019). Using a heterogeneous rheology model, Sasajima et al. (2019) indicated that the rapid interseismic subsidence in the last decade was caused by coupling at the deeper part of the plate boundary fault, which was previously hypothesized by several studies such as Nishimura (2014). As heterogeneous rheology explains the deformation mechanisms in interseismic (Sasajima et al. 2019) and short-term postseismic period (e.g., Agata et al. 2019; Muto et al. 2019; Dhar et al. 2022), it may also help explain the long-term deformation, which can contribute to the solution of the above-mentioned paradox.

### 6.3 Toward much finer rheological heterogeneities in coming decades

As suggested in previous studies (Muto et al. 2016, 2019; Dhar et al. 2022), small-scale rheological heterogeneity can provide valuable insights into the relative contributions of VR and AS to ground deformation after the 2011 Tohoku-oki earthquake. To capture small-scale rheology, denser geodetic observations than those of GEONET are required. Recently, Japanese telecommunication companies have been investing in building a private GNSS network to obtain high-precision location data for various applications ranging from automobiles to agriculture to public surveys. In November 2019, SoftBank Corp. constructed a network of more than 3300 stations across Japan (average spatial density of 6–7 km), which is 2.5 times the number of GEONET stations (Ohta and Ohzono 2022). By comparing with GEONET, Ohta and Ohzono (2022) demonstrated the usefulness of this private GNSS networks for monitoring crustal deformation.

Space-borne synthetic aperture radar (SAR) data can also illuminate crustal deformation at high spatial resolutions. Interferometry SAR (InSAR) time series is widely used to detect centimeter-scale volcanic deformation (Pritchard and Simons 2004). Over the past few decades, InSAR time series with GNSS observations have been deployed to monitor transient postseismic deformation (e.g., Ryder et al. 2007; Moore et al. 2017). In addition to the coseismic subsidence around the Quaternary volcanoes reported by Takada and Fukushima (2013), Fukushima et al. (2013) captured the coseismic displacements of the 2011 Mw 6.6 Iwaki earthquake that occurred on April 11 using data from the Japanese ALOS satellite. Recently, Morishita and Kobayashi (2022) combined InSAR, split-bandwidth interferometry, and the pixel offset method to derive the 3-D coseismic deformation for the 2016 Kumamoto earthquake and the 2016 Central Tottori earthquake with an observational error of a few centimeters. With the advancement of SAR technology (e.g., data acquisition by Landsat from 2013 onward), it is possible to capture the recent postseismic crustal deformation of the Tohoku region at a high resolution in the coming decades. Combined observations from dense GNSS networks and InSAR images may provide further insight into the rheological heterogeneity of NE Japan with unprecedented resolution. They may help illuminate geodynamic processes with finer resolutions such as the detailed nature of the recovery of plate coupling after the megathrust earthquake, as well as mitigate future hazards from inland earthquakes triggered by postseismic deformation (e.g., Freed and Lin 2001).

## 7 Conclusions

We piece together the rheological heterogeneities of the Japan subduction zone inferred from the dense observations of the postseismic deformation of the 2011 Tohoku-oki earthquake. Over the last decade, numerous postseismic models have combined VR and AS to explain the geodetic observations. Whereas horizontal GNSS observations provide the boundary conditions (lithosphere–asthenosphere system with subducting slab of finite thickness, viscosity contrast between the mantle wedge and oceanic mantle) required for post-seismic modeling, vertical observations play a significant role in resolving the heterogeneous rheology in the Japan subduction zone. The vertical motion captured by the dense geodetic network reveals low-viscosity bodies beneath the Quaternary volcanoes, which can be correlated to other geophysical observations such as seismic tomography, inland seismicity, and heat flow observations. The vertical motion along the Miyagi and Fukushima forearcs inferred the elastic/high-viscous “cold nose,” which was also inferred by the thermo-petrological model. Depth-dependent models or power-law rheology provide a unique perspective of understanding the viscoelastic mantle through rheological stratification. It thus enables us to illuminate the ambient mantle condition (for instance, water stratification) in a transform or subduction zone. In a power-law model, the rheological heterogeneities, such as depth-dependent viscosity, LVZ, and cold nose, contribute to the inland vertical pattern of postseismic surface deformation. Moreover, the weak oceanic asthenosphere plays a significant role in the landward deformation of the trench. The geometry and rheological properties of these rheological heterogeneities control the amplitude of the modeled deformation, enabling us to explain the geodetic observations more quantitatively. The rheological heterogeneities beneath NE Japan may further help us to understand the relative contributions of VR and AS and their role in the decade-scale subduction zone earthquake cycle. Furthermore, evaluating the extinction of local AS is necessary to understand the recovery of plate coupling adequately. Such site-specific or heterogeneous AS may produce vertical deformation similar to localized viscoelastic deformation. Further development of dense observational networks and heterogeneous postseismic models that can reveal local crustal deformation will contribute to image a detailed picture of the recovery of plate coupling.

### Abbreviations

AS	Afterslip
CNE	Cold-nose edge
GNSS	Global Navigation Satellite System
GNSS-A	GNSS-Acoustic
JCG	Japan Coast Guard

LVZ	Low-viscosity zone
THK	Tohoku University inland GNSS sites
TU GNSS-A	Tohoku University GNSS-A sites
VR	Viscoelastic relaxation

## Supplementary Information

The online version contains supplementary material available at <https://doi.org/10.1186/s40645-023-00539-1>.

**Additional file 1. Text S1.** Calculation of effective viscosity for power-law models. **Figure S1.** Seafloor GNSS-A sites at Japan trench. **Figure S2.** The effect of rheological and thermal parameters on one-dimensional viscosity profile. **Table S1.** Framework details and rheology of base model. **Table S2.** Depth-dependent viscosity models for mantle wedge. **Table S3.** Depth-dependent viscosity models for oceanic mantle. **Table S4.** Parameters for LVZ models.

### Acknowledgements

We acknowledge Sylvain Barbot, Yan Hu, Hiraku Iwamori, James Moore, Tomomi Okada, Takeshi Sagiya, Bunichiro Shibazaki, Youichiro Takada, Takeyoshi Yoshida, and Kelin Wang for their helpful comments and discussions. We thank Roland Bürgmann (the Editor) and two anonymous reviewers for their comments and suggestions. We also thank Editage ([www.editage.com](http://www.editage.com)) for English language editing. Figures 1, 2, 4–8 are created using GMT6.0 (Wessel et al. 2019).

### Author contributions

JM contributed to conceptualization; SD and JM contributed to writing—original draft preparation; SD, JM, YO, and TI contributed to writing—review and editing. All authors read and approved the final manuscript.

### Funding

This study was funded by the Ministry of Education, Culture, Sport, Science, and Technology (MEXT) of Japan under its Earthquake, and Volcano Hazards Observation and Research Program.

### Availability of data and materials

No new data have been generated in this study. The GEONET data are available from the Geospatial Information Authority of Japan (<http://terras.gsi.go.jp/>).

### Declarations

#### Competing interests

The authors declare that they have no competing interest.

Received: 6 September 2022 Accepted: 9 February 2023

Published online: 28 February 2023

### References

- Agata R, Barbot SD, Fujita K, Hyodo M, Iinuma T, Nakata R, Ichimura T, Hori T (2019) Rapid mantle flow with power-law creep explains deformation after the 2011 Tohoku mega-quake. *Nat Commun* 10(1):1–11. <https://doi.org/10.1038/s41467-019-08984-7>
- Ashby M, Duval P (1985) The creep of polycrystalline ice. *Cold Reg Sci Technol* 11(3):285–300. [https://doi.org/10.1016/0165-232X\(85\)90052-7](https://doi.org/10.1016/0165-232X(85)90052-7)
- Ban M, Takahashi K, Horie T, Toya N (2005) Petrogenesis of mafic inclusions in rhyolitic lavas from Narugo volcano, northeastern Japan. *J Petrol* 46(8):1543–1563. <https://doi.org/10.1093/petrology/egi025>
- Barbot S (2018) Asthenosphere flow modulated by megathrust earthquake cycles. *Geophys Res Lett* 45(12):6018–6031. <https://doi.org/10.1029/2018GL078197>
- Barbot S (2020) Frictional and structural controls of seismic super-cycles at the Japan trench. *Earth Planets Space* 72(1):1–25. <https://doi.org/10.1186/s40623-020-01185-3>

- Barbot S, Moore JD, Lambert V (2017) Displacement and stress associated with distributed anelastic deformation in a half-space. *Bull Seismol Soc Am* 107(2):821–855. <https://doi.org/10.1785/0120160237>
- Bürgmann R, Dresen G (2008) Rheology of the lower crust and upper mantle: evidence from rock mechanics, geodesy, and field observations. *Annu Rev Earth Planet Sci* 36:531–567. <https://doi.org/10.1146/annurev.earth.36.031207.124326>
- Carte, NL, Kirby SH (1978) Transient creep and semibrittle behavior of crystalline rocks. In: *Rock friction and earthquake prediction*. Springer, pp 807–839
- Carter NL, Ave'Lallemant HG (1970) High temperature flow of dunite and peridotite. *Geol Soc Am Bull* 81(8):2181–2202. [https://doi.org/10.1130/0016-7606\(1970\)81\[2181:HTFODA\]2.0.CO;2](https://doi.org/10.1130/0016-7606(1970)81[2181:HTFODA]2.0.CO;2)
- Carter NL, Tsenn MC (1987) Flow properties of continental lithosphere. *Tectonophysics* 136(1–2):27–63. [https://doi.org/10.1016/0040-1951\(87\)90333-7](https://doi.org/10.1016/0040-1951(87)90333-7)
- Chopra PN (1997) High-temperature transient creep in olivine rocks. *Tectonophysics* 279(1–4):93–111. [https://doi.org/10.1016/S0040-1951\(97\)00134-0](https://doi.org/10.1016/S0040-1951(97)00134-0)
- Dhar S, Muto J, Ito Y, Miura S, Moore JD, Ohta Y, Iinuma T (2022) Along-arc heterogeneous rheology inferred from post-seismic deformation of the 2011 Tohoku-oki earthquake. *Geophys J Int* 230(1):202–215. <https://doi.org/10.1093/gji/ggac063>
- Diao F, Xiong X, Wang R, Zheng Y, Walter TR, Weng H, Li J (2014) Overlapping post-seismic deformation processes: Afterslip and viscoelastic relaxation following the 2011 Mw 9.0 Tohoku Japan earthquake. *Geophys J Int* 196(1):218–229. <https://doi.org/10.1093/gji/ggt376>
- Durham W, Goetze C, Blake B (1977) Plastic flow of oriented single crystals of olivine: 2. observations and interpretations of the dislocation structures. *J Geophys Res* 82(36):5755–5770. <https://doi.org/10.1029/JB082i036p05755>
- Freed AM, Bürgmann R (2004) Evidence of power-law flow in the Mojave desert mantle. *Nature* 430(6999):548–551. <https://doi.org/10.1038/nature02784>
- Freed AM, Lin J (2001) Delayed triggering of the 1999 Hector Mine earthquake by viscoelastic stress transfer. *Nature* 411(6834):180–183. <https://doi.org/10.1038/35075548>
- Freed AM, Bürgmann R, Calais E, Freymueller J, Hreinsdóttir S (2006) Implications of deformation following the 2002 Denali, Alaska, earthquake for postseismic relaxation processes and lithospheric rheology. *J Geophys Res Solid Earth*. <https://doi.org/10.1029/2005JB003894>
- Freed AM, Herring T, Bürgmann R (2010) Steady-state laboratory flow laws alone fail to explain postseismic observations. *Earth Planet Sci Lett* 300(1–2):1–10. <https://doi.org/10.1016/j.epsl.2010.10.005>
- Freed AM, Hirth G, Behn MD (2012) Using short-term postseismic displacements to infer the ambient deformation conditions of the upper mantle. *J Geophys Res Solid Earth*. <https://doi.org/10.1029/2011JB008562>
- Freed AM, Hashima A, Becker TW, Okaya DA, Sato H, Hatanaka Y (2017) Resolving depth-dependent subduction zone viscosity and afterslip from postseismic displacements following the 2011 Tohoku-oki, Japan earthquake. *Earth Planet Sci Lett* 459:279–290. <https://doi.org/10.1016/j.epsl.2016.11.040>
- Fukuda J, Johnson KM (2021) Bayesian inversion for a stress-driven model of afterslip and viscoelastic relaxation: Method and application to post-seismic deformation following the 2011 Mw 9.0 Tohoku-Oki earthquake. *J Geophys Res Solid Earth* 126(5):2020–021620. <https://doi.org/10.1029/2020JB021620>
- Fukushima Y, Takada Y, Hashimoto M (2013) Complex ruptures of the 11 April 2011 Mw 6.6 Iwaki earthquake triggered by the 11 March 2011 Mw 9.0 Tohoku earthquake, Japan complex ruptures of Mw 6.6 Iwaki earthquake triggered by Mw 9.0 Tohoku earthquake. *Bull Seismol Soc Am* 103(2B):1572–1583. <https://doi.org/10.1785/0120120140>
- Furukawa Y (1993) Depth of the decoupling plate interface and thermal structure under arcs. *J Geophys Res Solid Earth* 98(B11):20005–20013. <https://doi.org/10.1029/93JB02020>
- Goetze C, Evans B (1979) Stress and temperature in the bending lithosphere as constrained by experimental rock mechanics. *Geophys J Int* 59(3):463–478. <https://doi.org/10.1111/j.1365-246X.1979.tb02567.x>
- Han S-C, Sauber J, Luthcke SB, Ji C, Pollitz FF (2008) Implications of postseismic gravity change following the great 2004 Sumatra-Andaman earthquake from the regional harmonic analysis of GRACE intersatellite tracking data. *J Geophys Res Solid Earth*. <https://doi.org/10.1029/2008JB005705>
- Hansen LN, Kumamoto KM, Thom CA, Wallis D, Durham WB, Goldsby DL, Breithaupt T, Meyers CD, Kohlstedt DL (2019) Low-temperature plasticity in olivine: Grain size, strain hardening, and the strength of the lithosphere. *J Geophys Res Solid Earth* 124(6):5427–5449. <https://doi.org/10.1029/2018JB016736>
- Hansen LN, Wallis D, Breithaupt T, Thom CA, Kempton I (2021) Dislocation creep of olivine: backstress evolution controls transient creep at high temperatures. *J Geophys Res Solid Earth* 126(5):2020–021325. <https://doi.org/10.1029/2020JB021325>
- Hanson DR, Spetzler HA (1994) Transient creep in natural and synthetic, iron-bearing olivine single crystals: Mechanical results and dislocation microstructures. *Tectonophysics* 235(4):293–315. [https://doi.org/10.1016/0040-1951\(94\)90191-0](https://doi.org/10.1016/0040-1951(94)90191-0)
- Hasegawa A, Nakajima J, Umino N, Miura S (2005) Deep structure of the northeastern Japan arc and its implications for crustal deformation and shallow seismic activity. *Tectonophysics* 403(1–4):59–75. <https://doi.org/10.1016/j.tecto.2005.03.018>
- Hasegawa A, Nakajima J, Uchida N, Okada T, Zhao D, Matsuzawa T, Umino N (2009) Plate subduction, and generation of earthquakes and magmas in Japan as inferred from seismic observations: an overview. *Gondwana Res* 16(3–4):370–400. <https://doi.org/10.1016/j.gr.2009.03.007>
- Hearn E, McClusky S, Ergintav S, Reilinger R (2009) Izmit earthquake postseismic deformation and dynamics of the north Anatolian fault zone. *J Geophys Res Solid Earth*. <https://doi.org/10.1029/2008JB006026>
- Heki K, Miyazaki S, Tsuji H (1997) Silent fault slip following an interplate thrust earthquake at the Japan trench. *Nature* 386(6625):595–598. <https://doi.org/10.1038/386595a0>
- Hirschmann MM (2010) Partial melt in the oceanic low velocity zone. *Phys Earth Planet Inter* 179(1–2):60–71. <https://doi.org/10.1016/j.pepi.2009.12.003>
- Hirth G, Kohlstedt D (2003) Inside the subduction factory. Rheology of the upper mantle and the mantle wedge: a view from the experimentalists. *Geophys Monogr Ser* 138:83–105
- Hoechner A, Sobolev SV, Einarsson I, Wang R (2011) Investigation on afterslip and steady state and transient rheology based on postseismic deformation and geoid change caused by the Sumatra 2004 earthquake. *Geochem Geophys Geosyst*. <https://doi.org/10.1029/2010GC003450>
- Honsho C, Kido M, Tomita F, Uchida N (2019) Offshore postseismic deformation of the 2011 Tohoku earthquake revisited: Application of an improved GPS-acoustic positioning method considering horizontal gradient of sound speed structure. *J Geophys Res Solid Earth* 124(6):5990–6009. <https://doi.org/10.1029/2018JB017135>
- Hsu Y-J, Simons M, Avouac J-P, Galetzka J, Sieh K, Chlieh M, Natawidjaja D, Prawirodirdjo L, Bock Y (2006) Frictional afterslip following the 2005 Nias-Simeulue earthquake. *Sumatra Science* 312(5782):1921–1926. <https://doi.org/10.1126/science.1126960>
- Hu Y, Bürgmann R, Freymueller JT, Banerjee P, Wang K (2014) Contributions of poroelastic rebound and a weak volcanic arc to the postseismic deformation of the 2011 Tohoku earthquake. *Earth Planets Space* 66(1):1–10. <https://doi.org/10.1186/1880-5981-66-106>
- Hu Y, Bürgmann R, Uchida N, Banerjee P, Freymueller JT (2016) Stress-driven relaxation of heterogeneous upper mantle and time-dependent afterslip following the 2011 Tohoku earthquake. *J Geophys Res Solid Earth* 121(1):385–411. <https://doi.org/10.1002/2015JB012508>
- Huang Z, Zhao D, Wang L (2011) Seismic heterogeneity and anisotropy of the Honshu arc from the Japan trench to the Japan sea. *Geophys J Int* 184(3):1428–1444. <https://doi.org/10.1111/j.1365-246X.2011.04934.x>
- Iinuma T, Ohzono M, Ohta Y, Miura S, Kasahara M, Takahashi H, Sagiya T, Matsushima T, Nakao S, Ueki S et al (2009) Aseismic slow slip on an inland active fault triggered by a nearby shallow event, the 2008 Iwate-Miyagi Nairiku earthquake (Mw 6.8). *Geophys Res Lett*. <https://doi.org/10.1029/2009GL040063>
- Iinuma T, Hino R, Kido M, Inazu D, Osada Y, Ito Y, Ohzono M, Tsushima H, Suzuki S, Fujimoto H et al (2012) Coseismic slip distribution of the 2011 off the Pacific coast of Tohoku earthquake (M9.0) refined by means of seafloor geodetic data. *J Geophys Res Solid Earth*. <https://doi.org/10.1029/2012JB009186>
- Iinuma T, Hino R, Uchida N, Nakamura W, Kido M, Osada Y, Miura S (2016) Seafloor observations indicate spatial separation of coseismic and



- postseismic slips in the 2011 Tohoku earthquake. *Nat Commun* 7(1):1–9. <https://doi.org/10.1038/ncomms13506>
- Imakiire T, Koarai M (2012) Wide-area land subsidence caused by “the 2011 off the Pacific coast of Tohoku earthquake.” *Soils Found* 52(5):842–855. <https://doi.org/10.1016/j.sandf.2012.11.007>
- Ingleby T, Wright T (2017) Omori-like decay of postseismic velocities following continental earthquakes. *Geophys Res Lett* 44(7):3119–3130. <https://doi.org/10.1002/2017GL072865>
- Ishikawa T, Yokota Y, Watanabe S-i, Nakamura Y (2020) History of on-board equipment improvement for GNSS-A observation with focus on observation frequency. *Front Earth Sci* 8:150. <https://doi.org/10.3389/feart.2020.00150>
- Iwamori H, Zhao D (2000) Melting and seismic structure beneath the north-east Japan arc. *Geophys Res Lett* 27(3):425–428. <https://doi.org/10.1029/1999GL010917>
- James TS, Clague JJ, Wang K, Hutchinson I (2000) Postglacial rebound at the northern Cascadia subduction zone. *Quatern Sci Rev* 19(14–15):1527–1541. [https://doi.org/10.1016/S0277-3791\(00\)00076-7](https://doi.org/10.1016/S0277-3791(00)00076-7)
- Karato S-i (2008) *Deformation of Earth Materials: An Introduction to the Rheology of Solid Earth*. Cambridge University Press, Cambridge. <https://doi.org/10.1017/CBO9780511804892>
- Karato S-i (2012) On the origin of the asthenosphere. *Earth Planet Sci Lett* 321:95–103. <https://doi.org/10.1016/j.epsl.2012.01.001>
- Karato S-i (2021) A theory of inter-granular transient dislocation creep: Implications for the geophysical studies on mantle rheology. *J Geophys Res Solid Earth* 126(10):2021–022763. <https://doi.org/10.1029/2021JB022763>
- Karato S-i, Jung H (1998) Water, partial melting and the origin of the seismic low velocity and high attenuation zone in the upper mantle. *Earth Planet Sci Lett* 157(3–4):193–207. [https://doi.org/10.1016/S0012-821X\(98\)00034-X](https://doi.org/10.1016/S0012-821X(98)00034-X)
- Karato S-i, Jung H (2003) Effects of pressure on high-temperature dislocation creep in olivine. *Phil Mag* 83(3):401–414. <https://doi.org/10.1080/0141861021000025829>
- Karato S-i (1998) Micro-physics of post glacial rebound. In: *Retrospective Collection*, vol 24, pp 351–364. *Trans Tech Publ*
- Kato T, El-Fiky G, Oware EN, Miyazaki S (1998) Crustal strains in the Japanese islands as deduced from dense GPS array. *Geophys Res Lett* 25(18):3445–3448. <https://doi.org/10.1029/98GL02693>
- Kawakatsu H, Kumar P, Takei Y, Shinohara M, Kanazawa T, Araki E, Suyehiro K (2009) Seismic evidence for sharp lithosphere-asthenosphere boundaries of oceanic plates. *Science* 324(5926):499–502. <https://doi.org/10.1126/science.1169499>
- Kido M, Osada Y, Fujimoto H, Hino R, Ito Y (2011) Trench-normal variation in observed seafloor displacements associated with the 2011 Tohoku-oki earthquake. *Geophys Res Lett*. <https://doi.org/10.1029/2011GL050057>
- Kido M, Fujimoto H, Hino R, Ohta Y, Osada Y, Iinuma T, Azuma R, Wada I, Miura S, Suzuki S, et al (2015) Progress in the project for development of GPS/acoustic technique over the last 4 years. In: *International symposium on geodesy for earthquake and natural hazards (GENAH)*, pp 3–10. <https://doi.org/10.1007/13452015127>. Springer
- Kirby SH (1983) Rheology of the lithosphere. *Rev Geophys* 21(6):1458–1487. <https://doi.org/10.1029/RG021i006p01458>
- Kirby S, Kronenberg A (1987) Rheology of the lithosphere: Selected topics. *Rev Geophys* 25(6):1219–1244. <https://doi.org/10.1029/RG025i006p01219>
- Kohlstedt D, Evans B, Mackwell S (1995) Strength of the lithosphere: Constraints imposed by laboratory experiments. *J Geophys Res Solid Earth* 100(B9):17587–17602. <https://doi.org/10.1029/95JB01460>
- Lambert V, Barbot S (2016) Contribution of viscoelastic flow in earthquake cycles within the lithosphere-asthenosphere system. *Geophys Res Lett* 43(19):10–142. <https://doi.org/10.1002/2016GL070345>
- Li S, Chen L (2022) Elastic slab in viscoelastic mantle: Effects on determining megathrust slip and mantle viscosity during postseismic and interseismic phases. *J Geophys Res Solid Earth*. <https://doi.org/10.1029/2022JB024730>
- Liu X, Zhao D (2016) P and S wave tomography of Japan subduction zone from joint inversions of local and teleseismic travel times and surface-wave data. *Phys Earth Planet Inter* 252:1–22. <https://doi.org/10.1016/j.pepi.2016.01.002>
- Liu X, Zhao D, Li S, Wei W (2017) Age of the subducting Pacific slab beneath east Asia and its geodynamic implications. *Earth Planet Sci Lett* 464:166–174. <https://doi.org/10.1016/j.epsl.2017.02.024>
- Luo H, Wang K (2021) Postseismic geodetic signature of cold forearc mantle in subduction zones. *Nat Geosci* 14(2):104–109. <https://doi.org/10.1038/s41561-020-00679-9>
- Luo H, Wang K (2022) Finding simplicity in the complexity of postseismic coastal uplift and subsidence following great subduction earthquakes. *J Geophys Res Solid Earth* 127(10):2022–024471. <https://doi.org/10.1029/2022JB024471>
- Mackwell S, Kohlstedt D, Paterson M (1985) The role of water in the deformation of olivine single crystals. *J Geophys Res Solid Earth* 90(B13):11319–11333. <https://doi.org/10.1029/JB090B13p11319>
- Marone CJ, Scholtz C, Bilham R (1991) On the mechanics of earthquake afterslip. *J Geophys Res Solid Earth* 96(B5):8441–8452. <https://doi.org/10.1029/91JB00275>
- Masuti S, Barbot S (2021) MCMC inversion of the transient and steady-state creep flow law parameters of dunite under dry and wet conditions. *Earth Planets Space* 73(1):1–21. <https://doi.org/10.1186/s40623-021-01543-9>
- Masuti S, Barbot SD, Karato S-i, Feng L, Banerjee P (2016) Upper-mantle water stratification inferred from observations of the 2012 Indian ocean earthquake. *Nature* 538(7625):373–377. <https://doi.org/10.1038/nature19783>
- Masuti S, Karato S-i, Girard J, Barbot SD (2019) Anisotropic high-temperature creep in hydrous olivine single crystals and its geodynamic implications. *Phys Earth Planet Inter* 290:1–9. <https://doi.org/10.1016/j.pepi.2019.03.002>
- Matsumoto T, Yamada R, Iizuka S (2022) Heat flow data and thermal structure in Northeastern Japan. *Earth Planets Space* 74(1):1–38. <https://doi.org/10.1186/s40623-022-01704-4>
- Miyashita K (1987) A model of plate convergence in southwest Japan, inferred from leveling data associated with the 1946 Nankaido earthquake. *J Phys Earth* 35(6):449–467. <https://doi.org/10.4294/jpe.1952.35.449>
- Moore JD, Yu H, Tang C-H, Wang T, Barbot S, Peng D, Masuti S, Dauwels J, Hsu Y-J, Lambert V et al (2017) Imaging the distribution of transient viscosity after the 2016 Mw 7.1 Kumamoto earthquake. *Science* 356(6334):163–167. <https://doi.org/10.1126/science.aal3422>
- Morikami S, Mitsui Y (2020) Omori-like slow decay ( $p \sim 1$ ) of postseismic displacement rates following the 2011 Tohoku megathrust earthquake. *Earth Planets Space* 72(1):1–10. <https://doi.org/10.1186/s40623-020-01162-w>
- Morishita Y, Kobayashi T (2022) Three-dimensional deformation and its uncertainty derived by integrating multiple SAR data analysis methods. *Earth Planets Space* 74(1):1–19. <https://doi.org/10.1186/s40623-022-01571-z>
- Muto J (2011) Rheological structure of northeastern Japan lithosphere based on geophysical observations and rock mechanics. *Tectonophysics* 503(3–4):201–206. <https://doi.org/10.1016/j.tecto.2011.03.002>
- Muto J, Shibazaki B, Ito Y, Iinuma T, Ohzono M, Matsumoto T, Okada T (2013) Two-dimensional viscosity structure of the northeastern Japan islands arc-trench system. *Geophys Res Lett* 40(17):4604–4608. <https://doi.org/10.1002/grl.50906>
- Muto J, Shibazaki B, Iinuma T, Ito Y, Ohta Y, Miura S, Nakai Y (2016) Heterogeneous rheology controlled postseismic deformation of the 2011 Tohoku-oki earthquake. *Geophys Res Lett* 43(10):4971–4978. <https://doi.org/10.1002/2016GL068113>
- Muto J, Moore J, Barbot S, Iinuma T, Ohta Y, Iwamori H (2019) Coupled afterslip and transient mantle flow after the 2011 Tohoku earthquake. *Sci Adv* 5(9):1164. <https://doi.org/10.1126/sciadv.aaw1164>
- Nakajima J, Hasegawa A (2006) Anomalous low-velocity zone and linear alignment of seismicity along it in the subducted Pacific slab beneath Kanto, Japan: Reactivation of subducted fracture zone? *Geophys Res Lett*. <https://doi.org/10.1029/2006GL026773>
- Nakajima J, Hasegawa A (2007) Subduction of the Philippine Sea plate beneath southwestern Japan: Slab geometry and its relationship to arc magmatism. *J Geophys Res Solid Earth*. <https://doi.org/10.1029/2005GL025053>
- Nakajima J, Shimizu J, Hori S, Hasegawa A (2006) Shear-wave splitting beneath the southwestern Kurile arc and northeastern Japan arc: A new insight into mantle return flow. *Geophys Res Lett*. <https://doi.org/10.1029/2005GL025053>

- Nakajima J, Hirose F, Hasegawa A (2009) Seismotectonics beneath the Tokyo metropolitan area, Japan: effect of slab-slab contact and overlap on seismicity. *J Geophys Res Solid Earth*. <https://doi.org/10.1029/2008JB006101>
- Nakajima J, Hada S, Hayami E, Uchida N, Hasegawa A, Yoshioka S, Matsuzawa T, Umino N (2013) Seismic attenuation beneath northeastern Japan: constraints on mantle dynamics and arc magmatism. *J Geophys Res Solid Earth* 118(11):5838–5855. <https://doi.org/10.1002/2013JB010388>
- Nishimura T (2014) Pre-, co-, and post-seismic deformation of the 2011 Tohoku-oki earthquake and its implication to a paradox in short-term and long-term deformation. *J Disaster Res* 9(3):294–302. <https://doi.org/10.20965/jdr.2014.p0294>
- Nishimura T, Hirasawa T, Miyazaki S, Sagiya T, Tada T, Miura S, Tanaka K (2004) Temporal change of interplate coupling in northeastern Japan during 1995–2002 estimated from continuous GPS observations. *Geophys J Int* 157(2):901–916. <https://doi.org/10.1111/j.1365-246X.2004.02159.x>
- Nur A, Mavko G (1974) Postseismic viscoelastic rebound. *Science* 183(4121):204–206. <https://doi.org/10.1126/science.183.4121.204>
- Obara K, Kasahara K, Hori S, Okada Y (2005) A densely distributed high-sensitivity seismograph network in Japan: HI-net by national research institute for earth science and disaster prevention. *Rev Sci Instrum* 76(2):021301. <https://doi.org/10.1063/1.1854197>
- Ogawa Y, Ichiki M, Kanda W, Mishina M, Asamori K (2014) Three-dimensional magnetotelluric imaging of crustal fluids and seismicity around Naruko volcano, NE Japan. *Earth Planets Space* 66(1):1–13. <https://doi.org/10.1186/s40623-014-0158-y>
- Ohta Y, Ohzono M (2022) Potential for crustal deformation monitoring using a dense cell phone carrier global navigation satellite system network. *Earth Planets Space* 74(1):1–9. <https://doi.org/10.1186/s40623-022-01585-7>
- Ohta Y, Ohzono M, Miura S, Iinuma T, Tachibana K, Takatsuka K, Miyao K, Sato T, Umino N (2008) Coseismic fault model of the 2008 Iwate-Miyagi Nairiku earthquake deduced by a dense GPS network. *Earth Planets Space* 60(12):1197–1201. <https://doi.org/10.1186/BF03352878>
- Ohzono M, Ohta Y, Iinuma T, Miura S, Muto J (2012) Geodetic evidence of viscoelastic relaxation after the 2008 Iwate-Miyagi Nairiku earthquake. *Earth Planets Space* 64(9):759–764. <https://doi.org/10.5047/eps.2012.04.001>
- Okada T, Matsuzawa T, Hasegawa A (1995) Shear-wave polarization anisotropy beneath the north-eastern part of Honshu, Japan. *Geophys J Int* 123(3):781–797. <https://doi.org/10.1111/j.1365-246X.1995.tb06890.x>
- Okada Y, Kasahara K, Hori S, Obara K, Sekiguchi S, Fujiwara H, Yamamoto A (2004) Recent progress of seismic observation networks in Japan—HI-net, F-net, K-NET and KiK-net. *Earth Planets Space*. <https://doi.org/10.1186/BF03353076>
- Okada T, Matsuzawa T, Nakajima J, Uchida N, Yamamoto M, Hori S, Kono T, Nakayama T, Hirahara S, Hasegawa A (2014) Seismic velocity structure in and around the Naruko volcano, NE Japan, and its implications for volcanic and seismic activities. *Earth Planets Space* 66(1):1–10. <https://doi.org/10.1186/1880-5981-66-114>
- Omuralieva AM, Hasegawa A, Matsuzawa T, Nakajima J, Okada T (2012) Lateral variation of the cutoff depth of shallow earthquakes beneath the Japan islands and its implications for seismogenesis. *Tectonophysics* 518:93–105. <https://doi.org/10.1016/j.tecto.2011.11.013>
- Ota Y, Omura A (1991) Late Quaternary shorelines in the Japanese islands. *Quat Res* 30(3):175–186. <https://doi.org/10.4116/jaqua.30.175>
- Ozawa S, Nishimura T, Suito H, Kobayashi T, Tobita M, Imakiire T (2011) Coseismic and postseismic slip of the 2011 magnitude-9 Tohoku-oki earthquake. *Nature* 475(7356):373–376. <https://doi.org/10.1038/nature10227>
- Ozawa S, Nishimura T, Munekane H, Suito H, Kobayashi T, Tobita M, Imakiire T (2012) Preceding, coseismic, and postseismic slips of the 2011 Tohoku earthquake, Japan. *J Geophys Res Solid Earth*. <https://doi.org/10.1029/2011JB009120>
- Panet I, Pollitz F, Mikhailov V, Diament M, Banerjee P, Grijalva K (2010) Upper mantle rheology from GRACE and GPS postseismic deformation after the 2004 Sumatra-Andaman earthquake. *Geochem Geophys Geosyst*. <https://doi.org/10.1029/2009GC002905>
- Perfettini H, Avouac J (2014) The seismic cycle in the area of the 2011 Mw 9.0 Tohoku-oki earthquake. *J Geophys Res Solid Earth* 119(5):4469–4515. <https://doi.org/10.1002/2013JB010697>
- Pollitz FF (2003) Post-seismic relaxation theory on a laterally heterogeneous viscoelastic model. *Geophys J Int* 155(1):57–78. <https://doi.org/10.1046/j.1365-246X.2003.01980.x>
- Pollitz FF (2005) Transient rheology of the upper mantle beneath central Alaska inferred from the crustal velocity field following the 2002 Denali earthquake. *J Geophys Res Solid Earth*. <https://doi.org/10.1029/2005JB003672>
- Pollitz FF, Bürgmann R, Banerjee P (2006) Post-seismic relaxation following the great 2004 Sumatra-Andaman earthquake on a compressible self-gravitating earth. *Geophys J Int* 167(1):397–420. <https://doi.org/10.1111/j.1365-246X.2006.03018.x>
- Pollitz F, Banerjee P, Grijalva K, Nagarajan B, Bürgmann R (2008) Effect of 3-D viscoelastic structure on post-seismic relaxation from the 2004 Mw=9.2 Sumatra earthquake. *Geophys J Int* 173(1):189–204. <https://doi.org/10.1111/j.1365-246X.2007.03666.x>
- Post RL Jr (1977) High-temperature creep of Mt Burnet dunite. *Tectonophysics* 42(2–4):75–110. [https://doi.org/10.1016/0040-1951\(77\)90162-7](https://doi.org/10.1016/0040-1951(77)90162-7)
- Pritchard M, Simons M (2004) An InSAR-based survey of volcanic deformation in the central Andes. *Geochem Geophys Geosyst*. <https://doi.org/10.1029/2003GC000610>
- Pritchard M, Simons M (2006) An aseismic slip pulse in northern Chile and along-strike variations in seismogenic behavior. *J Geophys Res Solid Earth*. <https://doi.org/10.1029/2006JB004258>
- Qiu Q, Moore JD, Barbot S, Feng L, Hill EM (2018) Transient rheology of the Sumatran mantle wedge revealed by a decade of great earthquakes. *Nat Commun* 9(1):1–13. <https://doi.org/10.1038/s41467-018-03298-6>
- Riva RE, Govers R (2009) Relating viscosities from postseismic relaxation to a realistic viscosity structure for the lithosphere. *Geophys J Int* 176(2):614–624. <https://doi.org/10.1111/j.1365-246X.2008.04004.x>
- Ryder I, Parsons B, Wright TJ, Funning GJ (2007) Post-seismic motion following the 1997 Manyi Tibet earthquake: InSAR observations and modelling. *Geophys J Int* 169(3):1009–1027. <https://doi.org/10.1111/j.1365-246X.2006.03312.x>
- Sagiya T, Meneses-Gutierrez A (2022) Geodetic and geological deformation of the Island Arc in Northeast Japan revealed by the 2011 Tohoku earthquake. *Annu Rev Earth Planet Sci* 50(1):345–368. <https://doi.org/10.1146/annurev-earth-032320-074429>
- Sagiya T, Miyazaki S, Tada T (2000) Continuous GPS array and present-day crustal deformation of Japan. *Pure Appl Geophys* 157(11):2303–2322. <https://doi.org/10.1007/PL00022507>
- Sasajima R, Shibazaki B, Iwamori H, Nishimura T, Nakai Y (2019) Mechanism of subsidence of the northeast Japan forearc during the late period of a gigantic earthquake cycle. *Sci Rep* 9(1):1–13. <https://doi.org/10.1038/s41598-019-42169-y>
- Sato M, Ishikawa T, Ujihara N, Yoshida S, Fujita M, Mochizuki M, Asada A (2011) Displacement above the hypocenter of the 2011 Tohokuoki earthquake. *Science* 332(6036):1395–1395. <https://doi.org/10.1126/science.1207401>
- Shibazaki B (2023) Progress in modeling the Tohoku-oki megathrust earthquake cycle and associated crustal deformation processes. *Progress in Earth and Planetary Science* (in review)
- Shimamoto T (1993) Rheology of rocks and plate tectonics. *Comprehensive rock engineering, 1, Fundamentals*, 93–109. <https://cir.nii.ac.jp/crid/1571980074178730624>
- Shirzaei M, Bürgmann R, Uchida N, Hu Y, Pollitz F, Matsuzawa T (2014) Seismic versus aseismic slip: probing mechanical properties of the northeast Japan subduction zone. *Earth Planet Sci Lett* 406:7–13. <https://doi.org/10.1016/j.epsl.2014.08.035>
- Silver P, Mainprice D, Ismail W, Tommasi A, Barruol G (1999) Mantle structural geology from seismic anisotropy, pp 79–103. <https://hal.univ-reunion.fr/hal-01391514>
- Silverii F, Cheloni D, D'Agostino N, Selvaggi G, Boschi E (2014) Post-seismic slip of the 2011 Tohoku-oki earthquake from GPS observations: implications for depth-dependent properties of subduction megathrusts. *Geophys J Int* 198(1):580–596. <https://doi.org/10.1093/gji/ggu149>
- Smith B, Carpenter F (1987) Transient creep in orthosilicates. *Phys Earth Planet Inter* 49(3–4):314–324. [https://doi.org/10.1016/0031-9201\(87\)90033-1](https://doi.org/10.1016/0031-9201(87)90033-1)
- Suito H (2017) Importance of rheological heterogeneity for interpreting viscoelastic relaxation caused by the 2011 Tohoku-oki earthquake. *Earth Planets Space* 69(1):1–12. <https://doi.org/10.1186/s40623-017-0611-9>

- Suito H (2018) Current status of postseismic deformation following the 2011 Tohoku-oki earthquake. *J Disaster Res* 13(3):503–510. <https://doi.org/10.20965/jdr.2018.p0503>
- Suito H, Freymueller JT (2009) A viscoelastic and afterslip postseismic deformation model for the 1964 Alaska earthquake. *J Geophys Res Solid Earth*. <https://doi.org/10.1029/2008JB005954>
- Sun T, Wang K (2015) Viscoelastic relaxation following subduction earthquakes and its effects on afterslip determination. *J Geophys Res Solid Earth* 120(2):1329–1344. <https://doi.org/10.1002/2014JB011707>
- Sun T, Wang K, Iinuma T, Hino R, He J, Fujimoto H, Kido M, Osada Y, Miura S, Ohta Y et al (2014) Prevalence of viscoelastic relaxation after the 2011 Tohoku-oki earthquake. *Nature* 514(7520):84–87. <https://doi.org/10.1038/nature13778>
- Syracuse EM, van Keken PE, Abers GA (2010) The global range of subduction zone thermal models. *Phys Earth Planet Inter* 183(1–2):73–90. <https://doi.org/10.1016/j.pepi.2010.02.004>
- Takada Y, Fukushima Y (2013) Volcanic subsidence triggered by the 2011 Tohoku earthquake in Japan. *Nat Geosci* 6(8):637–641. <https://doi.org/10.1038/ngeo1857>
- Tamura Y, Tatsumi Y, Zhao D, Kido Y, Shukuno H (2002) Hot fingers in the mantle wedge: new insights into magma genesis in subduction zones. *Earth Planet Sci Lett* 197(1–2):105–116. [https://doi.org/10.1016/S0012-821X\(02\)00465-X](https://doi.org/10.1016/S0012-821X(02)00465-X)
- Tanaka A, Yamano M, Yano Y, Sasada M (2004) Geothermal gradient and heat flow data in and around Japan (I): Appraisal of heat flow from geothermal gradient data. *Earth Planets Space* 56(12):1191–1194. <https://doi.org/10.1186/BF03353339>
- Tang C-H, Hsu Y-J, Barbot S, Moore JD, Chang W-L (2019) Lower-crustal rheology and thermal gradient in the Taiwan orogenic belt illuminated by the 1999 Chi-Chi earthquake. *Sci Adv* 5(2):3287. <https://doi.org/10.1126/sciadv.aav3287>
- Tang C-H, Barbot S, Hsu Y-J, Wu Y-M (2020) Heterogeneous power-law flow with transient creep in southern California following the 2010 El Mayor-Cucapah earthquake. *J Geophys Res Solid Earth* 125(9):2020–019740. <https://doi.org/10.1029/2020JB019740>
- Tomita F, Kido M, Osada Y, Hino R, Ohta Y, Iinuma T (2015) First measurement of the displacement rate of the Pacific plate near the Japan trench after the 2011 Tohoku-oki earthquake using GPS/acoustic technique. *Geophys Res Lett* 42(20):8391–8397. <https://doi.org/10.1002/2015GL065746>
- Tomita F, Kido M, Ohta Y, Iinuma T, Hino R (2017) Along-trench variation in seafloor displacements after the 2011 Tohoku earthquake. *Sci Adv* 3(7):1700113. <https://doi.org/10.1126/sciadv.1700113>
- Tong P, Zhao D, Yang D (2012) Tomography of the 2011 Iwaki earthquake (M 7.0) and Fukushima nuclear power plant area. *Solid Earth* 3(1):43–51. <https://doi.org/10.5194/se-3-43-2012>
- Turcotte DL, Schubert G (1982) *Geodynamics applications of continuum physics to geological problems*. Wiley, New York
- Uchida N, Nakajima J, Wang K, Takagi R, Yoshida K, Nakayama T, Hino R, Okada T, Asano Y (2020) Stagnant forearc mantle wedge inferred from mapping of shear-wave anisotropy using S-net seafloor seismometers. *Nat Commun* 11(1):1–8. <https://doi.org/10.1038/s41467-020-19541-y>
- Wada I, Wang K (2009) Common depth of slab-mantle decoupling: Reconciling diversity and uniformity of subduction zones. *Geochem Geophys Geosyst*. <https://doi.org/10.1029/2009GC002570>
- Wang K, Hu Y, He J (2012) Deformation cycles of subduction earthquakes in a viscoelastic earth. *Nature* 484(7394):327–332. <https://doi.org/10.1038/nature11032>
- Wang K, Sun T, Brown L, Hino R, Tomita F, Kido M, Iinuma T, Kodaira S, Fujiwara T (2018) Learning from crustal deformation associated with the m9 2011 Tohoku-oki earthquake. *Geosphere* 14(2):552–571. <https://doi.org/10.1130/GES01531.1>
- Watanabe S-i, Sato M, Fujita M, Ishikawa T, Yokota Y, Ujihara N, Asada A (2014) Evidence of viscoelastic deformation following the 2011 Tohoku-oki earthquake revealed from seafloor geodetic observation. *Geophys Res Lett* 41(16):5789–5796. <https://doi.org/10.1002/2014GL061134>
- Watanabe S-i, Ishikawa T, Nakamura Y, Yokota Y (2021) Co- and post-seismic slip behaviors extracted from decadal seafloor geodesy after the 2011 Tohoku-oki earthquake. *Earth Planets Space* 73(1):1–12. <https://doi.org/10.1186/s40623-021-01487-0>
- Weiss JR, Qiu Q, Barbot S, Wright TJ, Foster JH, Saunders A, Brooks BA, Bevis M, Kendrick E, Ericksen TL et al (2019) Illuminating subduction zone rheological properties in the wake of a giant earthquake. *Sci Adv* 5(12):6720. <https://doi.org/10.1126/sciadv.aax6720>
- Wennerberg L, Sharp RV (1997) Bulk-friction modeling of afterslip and the modified Omori law. *Tectonophysics* 277(1–3):109–136. [https://doi.org/10.1016/S0040-1951\(97\)00081-4](https://doi.org/10.1016/S0040-1951(97)00081-4)
- Wessel P, Luis J, Uieda L, Scharroo R, Wobbe F, Smith WH, Tian D (2019) The generic mapping tools version 6. *Geochem Geophys Geosyst* 20(11):5556–5564. <https://doi.org/10.1029/2019GC008515>
- Yabe Y, Muto J, Ohzono M, Ohta Y, Iinuma T (2015) Rheological structure beneath NE Japan inferred from coseismic strain anomalies associated with the 2011 Tohoku-oki earthquake (Mw 9.0). In: International symposium on geodesy for earthquake and natural hazards (GENAH), pp 63–71. doi:[https://doi.org/10.1007/1345\\_2015\\_135](https://doi.org/10.1007/1345_2015_135). Springer
- Yamaguchi S, Miyazaki S, Hirahara K, Fukahata Y (2015) Afterslip and viscoelastic relaxation following the 2011 Tohoku-oki earthquake Mw9.0 inferred from inland GPS and seafloor GPS/acoustic data. *Geophys Res Lett* 42(1):66–73. <https://doi.org/10.1002/2014GL061735>
- Yamasaki T, Houseman GA (2012) The signature of depth-dependent viscosity structure in post-seismic deformation. *Geophys J Int* 190(2):769–784. <https://doi.org/10.1111/j.1365-246X.2012.05534.x>
- Yokota Y, Ishikawa T, Watanabe S-i (2018) Seafloor crustal deformation data along the subduction zones around Japan obtained by GNSS-A observations. *Scientific Data* 5(1):1–11. <https://doi.org/10.1038/sdata.2018.182>
- Yoshida T (2001) The evolution of arc magmatism in the NE Honshu arc, Japan. *Tohoku Geophys J* 36(2):131–149
- Zhao D (2012) Tomography and dynamics of Western-Pacific subduction zones. *Monogr Environ Earth Planets* 1(1):1–70. <https://doi.org/10.5047/meep.2012.00101.0001>
- Zhao D, Hasegawa A, Kanamori H (1994) Deep structure of Japan subduction zone as derived from local, regional, and teleseismic events. *J Geophys Res Solid Earth* 99(B11):22313–22329. <https://doi.org/10.1029/94JB01149>
- Zhao D, Yanada T, Hasegawa A, Umino N, Wei W (2012) Imaging the subducting slabs and mantle upwelling under the Japan islands. *Geophys J Int* 190(2):816–828. <https://doi.org/10.1111/j.1365-246X.2012.05550.x>

## Publisher's Note

Springer Nature remains neutral with regard to jurisdictional claims in published maps and institutional affiliations.

Submit your manuscript to a SpringerOpen® journal and benefit from:

- Convenient online submission
- Rigorous peer review
- Open access: articles freely available online
- High visibility within the field
- Retaining the copyright to your article

Submit your next manuscript at ► [springeropen.com](https://www.springeropen.com)